Project No. 10-911

Exploration and Modeling of Structural Changes in Waste Glass Under Corrosion

Fuel Cycle R&D

Dr. Carlo Pantano
Pennsylvania State University

In collaboration with:
Pacific Northwest National Laboratory

Kimberly Gray, Federal POC
John Vienna, Technical POC

NEUP Nuclear Energy University Programs
U.S. Department of Energy

ABSTRACT

The corrosion of nuclear waste glasses is a complex process involving adsorption, diffusion, ion-exchange, hydrolysis and precipitation of mineral alteration phases. These processes occur in parallel and their relative rates change significantly over the long term. Corrosion models are required to accurately reflect the long-term durability of vitrified high level waste so that geologic repositories can be designed to meet the targets of stability and security, and at the same time, make better utilization of the storage volume by increasing the density of HLW in the glass.

There are uncertainties in the existing corrosion models that have forced the current design of vitrified wasteforms to be extremely conservative. Of particular concern is the so-called residual dissolution rate which is observed in long-term laboratory leaching tests after 2-3 months. At this stage of the corrosion reaction, the combined effects of an altered surface layer and saturation of the contacting aqueous environment in silica reduce the initial dissolution rate by as much as 10,000 times. The residual rate is a critical design specification for both the wasteform and the repository, but validation of the atomic/molecular process or mechanism which controls this rate is still in question. Most workers agree that it is primarily dependent on the altered layer and its ability to limit mass transport, AND the effects of silica saturation in the contacting solution and its influence on the thermodynamic driving force for continued dissolution. This project aims to improve the understanding of these coupled phenomena by exploring new methods of analysis to probe atomic/molecular scale changes in both the altered layers and in the contacting solution, and thereby provide new information that can be used to update the existing long-term corrosion models.

This study focuses on the use of nuclear magnetic resonance (NMR) to provide detailed information about atomistic connectivity (bonding), proximity (spatial localization) and order (crystal nucleation) within the altered surface layers of glass powders after static dissolution at a high surface area to volume ratio for times up to 6 months. The NMR studies explored several glass compositions (AFCI, simplified SON68 and ISG) using isotopic enrichment or depletion of selected species in the glass (Si, B and Li) to follow their exchange with solution species, and vice-versa. Other experiments were performed with fibers under dynamic conditions, simpler binary and ternary glasses, neutron depth profiling (NDP), saturated glass solutions (SGS) and thermodynamic modeling with Geochemists Workbench to both supplement the NMR results and to more specifically address the role of solution saturation and mineral precipitation.

In addition to AFCI and SON68, simplified versions of these glasses were designed to reduce the complexity of the NMR spectra, including the international simplified glass (ISG) composition which was designed by a global coalition of researchers; very simple binary and ternary glasses were also employed to test specific effects. Some of these glasses were synthesized using raw materials enriched or depleted in Si, B or Li isotopes to follow their exchange with solution species. Saturated glass solutions (SGS) were made by total dissolution of finely ground powders to explore solution speciation effects at near equilibrium conditions.

Very high surface area to volume ratios (~100,000) were used in the reaction experiments to provide sufficient surface sensitivity in the NMR analyses. Cross-polarization NMR was able to detect the so-called hydrated interphase (between pristine glass and the gel layer) based on changes in composition and Q-speciation. All of the glass powders, except the ISG, showed the retention of Al in the gel layer; in contrast to its tetrahedral coordination in the bulk glass, it

established a six-fold coordination in the gel. Nevertheless, only the AFCI glass showed evidence of crystallinity in the altered layer under these highly saturated conditions; x-ray diffraction analysis was not able to identify the phase which disappeared at longer times). Interestingly, none of the glass fibers (in contrast to the glass powders) retained Al in the gel layer; this is likely due to the high fictive temperature and corresponding low density of the glass fibers compared to the crushed bulk glass, but needs to be confirmed. The fibers were also found to form thicker altered layers than the powders under otherwise comparable reaction conditions.

The glasses enriched and depleted in selected isotopes were used to follow the evolution of the gel layer over a time periods up to 6 months. In this work, we have used isotope exchange (so-called swapping experiments) to directly observe the dynamic equilibrium between silicic acid species in solution and Si species in and on the internal pore wall surfaces of the gel layer. Through the use of ^{29}Si magic angle spinning nuclear magnetic resonance (MAS NMR) and ^{1}H-^{29}Si cross-polarization (CP) MAS NMR, changes in the local coordination of Si in and on these surfaces could be detected. A time dependent trend towards higher coordination of Si in the gel is not surprising, but this work indicates that it is mediated by a rapid and continuous remodeling of the gel in concert with species in the bulk solution. Since these analyses were made under residual rate conditions, they confirm the continued structural evolution of the gel layer even when the dissolution rate is nearly constant. Although it was measured in a different glass, these results are consistent with our direct measurement of the gel layer density by neutron depth profiling (NDP) which was consistent with a porous permeable layer. The isotope exchange of B and Li were also explored with NMR and NDP, but interpretation of those results are uncertain at this time.

Finally, thermodynamic modeling of the saturated glass solutions that could play a role within the gel, at the hydrated interphase between bulk glass and the gel layer, or in the bulk solution, was initiated near the end of the program. Of particular interest was the evaluation of crystallization, and specifically, whether crystallization could drive dissolution under otherwise near equilibrium conditions. Simple binary, ternary and quaternary glasses were used to facilitate interpretation of the titration experiments and use of GeoChemists Workbench to model the experiments. The work is incomplete at this time, but for the simple experiments reported herein, equilibrium conditions between a mineral precipitate and the saturated solution in the presence of a gel phase were demonstrated. In one of these experiments, the dissolution of a 2 gram sample was observed to occur while the solution maintained a steady-state concentration. This approach is now being used to evaluate the dissolution behavior of other glasses, including more complex glasses, under near equilibrium conditions defined by mineral.

The silica gel that forms due to leaching, usually a relic of the original glass, is an important component of these systems that is still not well characterized. The swapping experiments monitored by NMR revealed that the gel is highly permeable and perhaps nano-particulate while wet. Its evolution occurs primarily through local transformation of the original glass structure rather than through precipitation from solution, while long term aging and structural coarsening of the gel occurs through surface adsorption-desorption reactions. Its' role in the nucleation of crystalline mineral phases warrants further study, but drying the gel for study likely alters its true characteristics. An important extension of the work reported here would be to use the SGS approach to create gel particles from glasses under controlled conditions, and use of physical and spectroscopic techniques such as NMR to characterize and monitor their evolution while wet.

Table of Contents

Definition of Common Acronyms

AFCI- Glass composition developed for the Advanced Fuel Cycle Initiative

CP- Cross-polarization

CPMG- Carr-Purcell-Meiboom-Gill

GWB- Geochemist Workbench

ICP-AES- Inductively coupled plasma-atomic emission spectroscopy

ISG- International simplified glass, based on SON68

LDS- Lithium disilicate

MAS- Magic angle spinning

NA- Natural abundance glass

NDP- Neutron depth profiling

NDS- Sodium disilicate

NLDS- Sodium lithium disilicate

NMR- Nuclear magnetic resonance

Q^n- Quaternary notation for ^{29}Si MAS NMR

SA1R- Simplified composition based on AFCI

SGS- Saturated Glass Solution

SON68- French nuclear waste composition

SPFT- Single-pass-flow-through

SS1R- Simplified composition based on SON68, containing Fe

SS2R- Simplified composition based on SON68, containing Zn

List of Tables

List of Figures

Figure 22. ^{1}H-^{29}Si CP-MAS NMR spectra of $SA1R_e$ glasses enriched in $^{28}SiO_2$. All signal derived from these glasses results from the dipolar interaction of ^{1}H nuclei with ^{29}Si from solution that has reacted with the $^{28}SiO_2$-enriched powder. Spectra have been normalized to remove the influence of variation in the sample mass and number of scans. (a) Samples have a 1-day equilibration period and (b) samples have equivalent initial corrosion and equilibration periods

Figure 23. ^{29}Si MAS NMR spectra of ISG_e glasses enriched in $^{28}SiO_2$. All signal derived from these glasses results from the interaction of ^{29}Si in solution with the $^{28}SiO_2$-enriched powder. Spectra with the same equilibration time have been normalized to remove the influence of variation in the sample mass and number of scans. (a) Samples have 1-day equilibration time and (b) samples have equilibration time equivalent to the initial corrosion time

Figure 24. ^{1}H-^{29}Si CP-MAS NMR spectra of ISG_e glasses enriched in $^{28}SiO_2$. All signal derived from these glasses results from the dipolar interaction of ^{1}H nuclei with ^{29}Si from solution that has reacted with the $^{28}SiO_2$-enriched powder. Spectra have been normalized to remove the influence of variation in the sample mass and number of scans. (a) Samples have a 1-day equilibration period and (b) samples have equivalent initial corrosion and equilibration periods

Figure 25. Depiction of the recondensation, where consecutive bonds form between aqueous silicic acid and the gel layer of the corroded glass powder

Figure 26. ^{1}H-^{23}Na CP-MAS NMR spectra of (a) SA1R and (b) AFCI. Samples were analyzed at 14.1 T with spinning speeds of 15 kHz. Spectra have been normalized to remove variation from the number of scans and sample mass

Figure 27. During hydrolysis, $^{[IV]}Al$ increases coordination to form $^{[VI]}Al$, which is subsequently incorporated into the gel layer. This figure is derived from work by Criscenti et al. on the dissolution of aluminosilicates

Figure 28. ^{11}B MAS NMR spectra of SA1Rd glasses containing $^{10}B_2O_3$ with a one-day equilibration time. All signal derived from these glasses results from the interaction of ^{11}B in solution with the $^{10}B_2O_3$-enriched powder or residual $^{11}B_2O_3$ in the glass. Spectra have been normalized to remove the influence of variation in the sample mass and number of scans. Samples were analyzed at 19.96 T with spinning speeds of 10 kHz

Figure 29. ^{1}H-^{11}B CP-MAS NMR spectra of SA1Rd glasses containing $^{10}B_2O_3$ with a one-day equilibration time. All signal derived from these glasses results from the dipolar interaction of ^{1}H nuclei with ^{11}B from solution that has reacted with the $^{10}B_2O_3$-enriched powder or residual $^{11}B_2O_3$ in the glass. Spectra have been normalized to remove the influence of variation in the sample mass and number of scans. Samples were analyzed at 19.96 T with spinning speeds of 10 kHz

Figure 30. ^{11}B MAS NMR spectra of ISGd glasses containing in $^{10}B_2O_3$ with (a) 1-day equilibration time and (b) equivalent initial corrosion and equilibration times. All signal derived from these glasses results from the interaction of ^{11}B in solution with

1. Introduction

Current solutions for radioactive waste storage include immobilization of the radioactive species in a borosilicate glass matrix by vitrification.[1] It is expected that long-term environmental exposure of vitreous waste forms will lead to changes in glass structure, especially when water breaches the burial sites and permeates any secondary barrier materials.[1] Ultimately, the interactions of water and glass will influence the stability of the waste form. Therefore, systematic characterization of the glass atomic structure, and especially the surface altered layers, are needed to provide insight into the mechanism of glass corrosion and the viability of specific glass compositions for use in the long-term stabilization of radionuclides. In this study, the term "alteration layers" is defined to include any material that has been changed from the pristine glass (with respect to either the composition or structure) due to the exposure to water, including the formation of secondary phases either from structural rearrangement or precipitation from solution.

Several physical mechanisms contribute to the time-dependent corrosion of multicomponent glasses. For convenience, the general behavior of glasses in static (non-refreshing) solutions can be broken into a series of steps that progress with time and ion concentration in solution.[1-6] The *initial* release of mass is due mainly to interdiffusion, with the subsequent contribution of hydrolysis proceeding rapidly as a consequence. During interdiffusion, water enters the glass matrix and soluble species such as sodium and boron are released to the surrounding solution. This step is usually assumed to be an ion-exchange between hydronium and modifier ions in the glass, but molecular water is also able to penetrate and react directly with the modifier site. Hydrolysis, on the other hand, refers to the attack of network bonds, especially Si-O-Si linkages, by water and hydroxyl species. The hydrolysis of silicate network bonds generates orthosilicic acid and its pH dependent ionization products (H_4SiO_4, $H_3SiO_4^-$, $HSiO_4^{2-}$), which are both released to solution and condensed at the surface. As the reaction proceeds, the release of ions to the bulk solution slows and an alteration layer forms on the surface. The alteration layer can be comprised of multiple sub-layers depending on the conditions and length of corrosion; a simplistic view is presented in Figure 1. Here we define three regions involved in corrosion: the pristine glass, the leached/hydrated glass network, and the silica gel layer. The silica gel layer is believed to form by a localized condensation at the corroding surface, although there is a corresponding saturation of the solution in silicic acid. During the formation of this altered surface layer, the rate of leaching and dissolution falls to a constant value known as the residual rate that persists, often indefinitely. After long times of aging, however, some glasses exhibit a renewal of the high initial dissolution rate. The origin and mechanism for this effect is unknown. One major objective of the structure studies reported here is to characterize atomic scale changes in the structure of the altered layers after long time aging in solution.

The low and constant dissolution rate observed in the residual rate regime has been attributed to both the increased level of soluble silicate species in the contacting solution and to the reduced transport kinetics through the surface alteration layers. It is not known which of these two coincident effects is rate-controlling; the former is termed the *affinity* or thermodynamic effect, while the latter is referred to as the *diffusion* or transport effect. Nevertheless, it is to be expected that the intrinsic reactivity of the glass surface will be significantly decreased by both the development of an altered surface layer and the saturation of

silicic acid in the contacting solution. Grambow and Muller [10] proposed a first order rate equation to describe glass dissolution kinetics based on the observation that the orthosilicic acid concentration controls the reaction rate.[1,7-11] The rate equation was derived from the work of Aagaard and Helgeson [12] on mineral dissolution, which show similar kinetic trends.[1,12,13] Independent evidence also suggests that one or more of the alteration layer(s) formed during the initial stages of glass corrosion can act as a diffusion barrier to slow down the interdiffusion reactions (Figure 1).[1] The complex nature of the altered layers, especially the amorphous water swollen gel layer, are difficult to characterize in-situ , and so there has been extensive debate about their role in the long-term leaching and dissolution of glass.[4,14-23] It seems likely that the extraction of glass samples from solution, and their drying and dehydration for analysis, redistributes and perhaps transforms the otherwise hydrated gel layer, in particular.

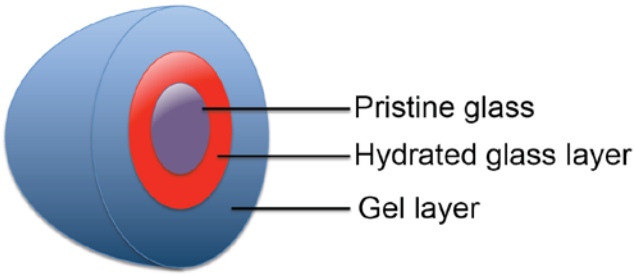

Figure 1. The surface alteration layer can be subdivided into two layers: the hydrated glass layer and the gel layer. The (partially) hydrated glass layer is the interface between the gel layer and pristine glass. The gel layer is in contact with the solution phase.

Of particular concern is the retention or *in situ* precipitation of components in the gel, which are dictated by solubility, thermodynamics, and kinetic considerations.[1,24] We define the interfacial region between the gel and pristine glass as the hydrated glass *network* where leaching and hydroxylation has occurred but breakdown and transformation of the original silicate network into a gel is still underway.[14] During the course of the reaction, however slow, mobile components in the hydrated glass layer will either be lost to solution or incorporate in the gel layer. The GRAAL model, which is under investigation as a theory for the prediction of nuclear waste glass behavior, uses a mathematically defined layer to restrict the transport of those components which control the glass dissolution rate.[1,4,25] That layer is proposed to be the hydrated glass and is postulated to limit water transport to the pristine glass. Gin et al. [4] successfully identified a one-micron thick hydrated glass layer by nanoscale-secondary-ion mass spectrometry (NanoSIMS). It is certainly possible that this layer explains the residual rate, but it does not yet explain the resumption of a high dissolution rate at long times.

One model for explaining the resumption of a high dissolution rate is the crystallization of stable mineral phases at long times, driven by the thermodynamic instability of the contacting solution which is saturated with respect to one or more crystalline phases. Crystalline secondary phases have, in fact, been observed to form on and within the silica gel layer.[4,16,18-20,26] Of particular interest here is the role of saturation and structural transformations within the altered layer itself, or whether this affinity effect is driven solely by the bulk contacting solution and its thermodynamics.

While previous work to study the evolution of glass corrosion rates has focused on the composition and growth rate of the alteration layers, their chemical structure and dynamics have not been well characterized.[4,14,15,27,28] This study, however, makes use of nuclear magnetic resonance (NMR) to provide detailed information about atomistic connectivity (bonding), proximity (spatial localization) and order (crystal nucleation) within the altered surface layers of glass powders after static dissolution at a high surface area to volume ratio for times up to 6 months. The NMR studies explored several glass compositions (AFCI, simplified SON68 and ISG) using isotopic enrichment or depletion of selected species in the glass (Si, B and Li) to follow their exchange with solution species, and vice-versa. Other experiments using simpler binary and ternary glasses, neutron depth profiling (NDP), saturated glass solutions (SGS) and thermodynamic modeling with Geochemists Workbench were used to both supplement the NMR results and to explore the affinity model.

This report is organized according to the original objectives and tasks of the project:

- 2.1 Selection of glass compositions
- 2.2 Synthesis of glasses and fibers
  - 2.2.1 AFCI
  - 2.2.2 SA1R, SS1R, and SS2R-Natural Abundance (NA)
  - 2.2.3 ISG-NA
  - 2.2.4 Isotopic glasses
  - 2.2.5 Fibers: SS1R, SS2R and ISG
  - 2.2.6 Simple glasses: LDS, NDS and NLDS
- 2.3 Reaction experiments
  - 2.3.1 SA1R (NA) and AFCI corrosion experiments
  - 2.3.2 Isotopic swap corrosion experiments
  - 2.3.3 Saturated glass solutions - SGS
- 2.4 Characterization of surface layer structure and evolution
  - 2.4.1 Glass composition effects on structure by NMR
  - 2.4.2 Fiber versus powder corrosion
  - 2.4.3 Evolution of surface structure by isotope exchange
  - 2.4.4 Counter diffusion effects by isotope exchange and NDP
- 2.5 Thermodynamic modeling of saturated glass solutions
  - 2.5.1 LDS experiments
  - 2.5.2 NDS experiments
  - 2.5.3 Aluminum doping experiments
  - 2.5.4 NLDS experiments
  - 2.5.5 Thermodynamic modeling with Geochemists Workbench
- 2.6 NMR database

2.0 Results and Discussion

2.1. Selection of Glass Compositions

SON68, an inactive form of the French R7T7 waste glass, has been well-studied by a variety of techniques (Table I).[1,4,5,8,9,11,15-19,25,29-44] Other glasses have been developed for different waste streams by various countries, but characterization has not been as extensive. Therefore, the first glass composition chosen for this study was developed by the United States Advanced Fuel Cycle Initiative (termed AFCI) (Table I). This composition was selected in order to make direct comparisons to SON68. AFCI and SON68 were modified to simplified versions in order to isolate the specific function of each component in the alteration process and reduce the glass complexity to derive information by characterization techniques (Table I). In order to generate the simplified compositions, components that would be maintained in the model glasses were identified. The remaining oxides were substituted by one of the "maintained oxides", depending on their typical function in a glass. For example, network modifying elements were replaced by other network modifiers. After the removed species were replaced, mass percentages were renormalized to one hundred. For SA1R (simplified AFCI), zirconium was kept as the model transition metal due to its substantial presence in initial compositions.

Three different simplified versions of SON68 were utilized: SS1R, SS2R, and ISG. The initial SS1R composition was selected based on the previous stipulations. The presence of paramagnetic iron in SS1R, however, prevented the success of certain NMR techniques. Therefore, iron was replaced with zinc in the SS2R composition. The validity of this substitution lies in the fact that zinc and iron should occupy roles in the glass structure. Finally, the international simplified glass (ISG) was chosen by a group of collaborators that could/will be studied by multiple laboratories around the globe using various techniques.

In addition to the simplified waste glass compositions, several simple binary, ternary and quaternary glasses were used to test the concept of crystallization driven glass dissolution (*affinity*). Li based glasses are found to create crystalline deposits in solution during their leaching and dissolution, whereas Na based glasses show less propensity to form crystals during their leaching and dissolution. This report includes data for $Na_2O{\cdot}2SiO_2$ (NDS), $Li_2O{\cdot}2SiO_2$ (LDS) and the ternary $0.5Na_2O{\cdot}0.5Li_2O{\cdot}2SiO_2$ (NLDS). Additional glasses in the Na and Li boroaluminosilicate system were also synthesized but their study is incomplete.

Table I: Glass compositions utilized in this work reported in weight percentage of oxides.

Component	**SON68 (wt %)**	**SS1R (wt %)**	**SS2R (wt %)**	**ISG (wt %)**	**AFCI (wt %)**	**SA1R (wt %)**
Ag_2O	0.03				0.04	
Al_2O_3	5.00	5.28	5.28	6.10	9.38	9.78
B_2O_3	14.14	14.94	14.94	17.30	9.65	10.06
BaO	0.62				0.85	
CaO	4.07	7.19	7.19	5.00	5.00	5.77
CdO	0.03				0.04	
Ce_2O_3	0.97				1.19	
Cr_2O_3	0.53					
Cs_2O	1.12				1.10	
Eu_2O_3					0.07	
Fe_2O_3	3.03	3.20				
Gd_2O_3					0.06	
La_2O_3	0.93	4.87	4.87		0.61	5.23
Li_2O	1.99	2.10	2.10		4.50	4.69
MnO_2	0.39					
MoO_3	1.78				1.50	
Na_2O	10.22	11.06	11.06	12.20	7.00	7.35
Nd_2O_3	2.04				2.01	
NiO	0.43					
P_2O_5	0.29					
PdO					0.01	
Pr_2O_3	0.46				0.56	
Rb_2O					0.16	
RhO_2					0.03	
RuO_2					0.08	
SeO_2					0.03	
SiO_2	45.85	48.44		56.20	53.67	55.93
Sm_2O_3					0.41	
SnO_2	0.02				0.03	
SrO	0.35				0.38	
TeO_2	0.23				0.25	
Y_2O_3	0.2				0.24	
ZnO	2.53		3.20			
ZrO_2	2.75	2.90	2.90	3.30	1.15	1.19

2.2. Synthesis of Glasses and Fibers.

2.2.1. AFCI

AFCI glass was prepared from reagent grade materials in 500 g batches at PNNL. The glass was melted for one hour at 1250 °C in a platinum-rhodium crucible. The glass melt was quenched (by pouring onto a stainless steel plate), crushed, and then re-melted for an additional hour. Detailed melting conditions and characterization of the glass can be found in Crum et al.[45]

2.2.2. SA1R, SS1R, and SS2R-Natural Abundance (NA)

Glasses were prepared at Penn State in 100-200 g batches using reagent-grade materials: Min-U-Sil SiO_2 from U.S. Silica, H_3BO_3 from Macron Chemicals, Na_2CO_3 from Alfa Aesar, $CaCO_3$ from Fisher Scientific, Li_2CO_3 from Mallinckrodt Incorporated, Al_2O_3 from Alfa Aesar, ZrO_2 from Potters Industries, ZnO from Fisher Scientific, Fe_2O_3 from Fisher Scientific, and La_2O_3 from Cerac Inc. Batch material was melted in a platinum crucible with a lid at 1275 °C for one hour and then quenched on a stainless steel plate. The glass was subsequently crushed in a tungsten carbide ball mill and re-melted for an additional hour at 1275 °C before final quenching.

2.2.3. ISG-NA

ISG glass was prepared according to the protocol outlined in Gin et al.[33] One-hundred gram batches were prepared from Min-U-Sil SiO_2 from U.S. Silica, H_3BO_3 from Macron Chemicals, Na_2CO_3 from Alfa Aesar, $CaCO_3$ from Fisher Scientific, Al_2O_3 from Alfa Aesar, and ZrO_2 from Potters Industries. Glasses were melted in platinum rhodium crucibles with lids at 1400 °C for 3 hours.

2.2.4. Isotopic Glasses

Two versions of isotopically enriched SA1R and ISG glasses were melted in 75 g batches. In the first version, the following isotopic materials were utilized: $^{6}Li_2CO_3$ (Cambridge Isotopes, 95.0 %), $^{10}B_2O_3$ (Isoflex USA, 99.59 %), and $^{29}SiO_2$ (Isoflex USA, 99.90 %). The isotopic materials in the second version glass were: $^{7}Li_2CO_3$ (Cambridge Isotopes, 99.94 %), $^{11}B_2O_3$ (Isoflex USA, 99.62 %), and $^{28}SiO_2$ (Isoflex USA, 99.98 %). The batch material for both SA1R glasses was melted in platinum crucibles with lids at 1300 °C for one hour. The glasses were poured on a stainless steel plate for quench cooling. Subsequently, the glasses were crushed in a tungsten carbide mill and re-melted for an additional hour. The batch materials for both ISG glasses were melted in platinum crucibles with lids at 1400 °C for 3 hours. The glasses were poured on a stainless steel plate for quench cooling.

2.2.5 Fibers: SS1R, SS2R and ISG

Simulated SON68 nuclear waste glasses (SS1R, SS2R and ISG) were re-melted in a single tip bushing to draw fiber with a diameter of the order 8-10 um. The fibers were wound on a Teflon mandrel and were subsequently vacuum-sealed for later use.

2.2.6 Simple Glasses: LDS, NDS and NLDS

Lithium disilicate (LDS), sodium disilicate (NDS), and sodium-lithium disilicate glasses were prepared in 300 g batches from the starting materials Li_2CO_3/SiO_2, Na_2CO_3/SiO_2, and $Na_2CO_3/Li_2CO_3/SiO_2$, respectively. Each composition was melted at 1275ºC for approximately one hour and then poured onto a stainless steel plate. The resulting glass slab was then crushed and remelted at the same temperature and time to ensure a homogenous melt. The second melt was poured onto a stainless steel slab containing square machined depressions to mold the slab. These features allow monolithic specimens to be easily cleaved from the main slab for other experiments on the as-cast or annealed surface. This slab was annealed at 500ºC for two hours and then cooled to 300ºC at a rate of 0.5ºC/min and then cooled to room temperature at a rate not exceeding 2ºC/min. Most of the annealed slabs were then crushed using a Retsch ® Vibratory Disc Mill RS 200 into a powder form with a particle size distribution ranging from hundreds of nanometers to millimeters. The powder was not sieved to a more precise size range, nor was the specific surface area of the powders measured since these experiments were not concerned with the determination of forward dissolution rates. However, for certain titration experiments involving precise quantities of starting glass, the powders were crushed even further to a very fine size to facilitate faster dissolution and subsequent saturation of the SGS.

2.3. Reaction Experiments

2.3.1. SA1R (NA) and AFCI Corrosion Experiments

Corrosion experiments were conducted according to the ASTM Standard 1285-02 Product Consistency Test.[46] A brief outline of those conditions will be described and further details can be found in the ASTM Standard. Glass was crushed into powder and sieved to less than 32 μm diameter particle size for AFCI and 20-32 μm particle size for SA1R. Fine particles were removed from SA1R powder through rinses with ASTM Type I water and ethanol. Powder was reacted in PFTA digestion bottles at 90 °C for various time periods with ASTM type I water and an original surface area to volume (S/V) ratio of 100,000 m^{-1}. Solution pH was not adjusted and therefore allowed to drift for the one month and five month exposure time period. An "accelerated" SA1R sample was corroded for one week using an initial solution pH of 11.5, adjusted with 5 M KOH. At the conclusion of the desired period, the powder samples were separated from the solution by vacuum filtration.

2.3.2. Isotopic Swap Corrosion Experiments

The isotopic swapping experiments are described schematically in Figure 2. The solutions were removed via syringes, but before the solution from vessel 1 was added to the powder in vessel 2, they and were passed through 0.45 micron syringe filters to remove particles that may have been suspended in solution. In order to minimize heat loss, swaps were completed rapidly and on a sheet of aluminum foil. Otherwise, the samples and reactions conditions were as outlined in Section 2.3.1. Sample nomenclature and associated experimental conditions can be found in Table II.

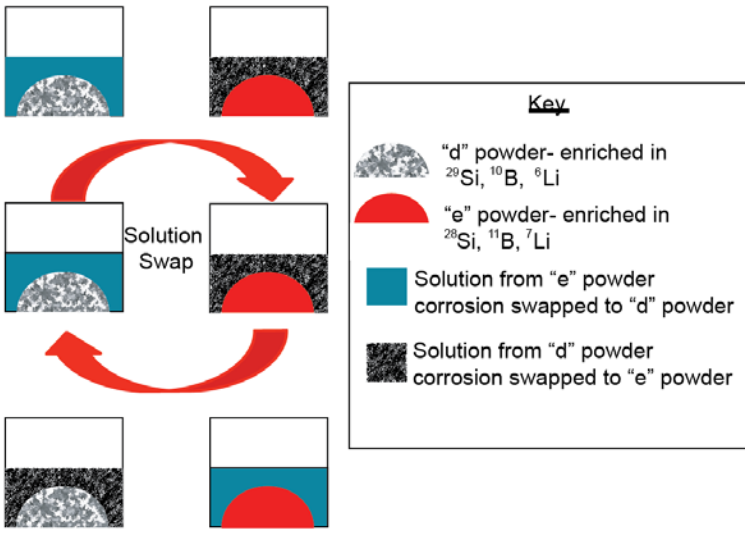

Figure 2. The "e" and "d" powders were melted with batch material containing selected isotopes. The "d" glass contained the low abundance isotopes (^{29}Si, ^{10}B, and ^{6}Li) while the "e" glass was enriched in the high abundance isotopes (^{28}Si, ^{11}B, and ^{7}Li). Reaction vessels with the e and d powders were held at 90 °C for a certain period of time under identical conditions. After the designated "initial time" of corrosion, the solutions containing isotopes from the e and d glasses were "swapped" to react in a solution containing isotopes from the other powder. The length of time after the solution exchange is designated the "equilibration time."

Table II. Nomenclature of swap samples. The first letter designates the glass composition (S=SA1R and I= ISG), the second letter designates the swap regime, and the lower case letter designates the isotopic enrichment. The samples with 1-day equilibration periods are italicized.

Sample Designation	Isotopic enrichment	"*initial time*" before swap (days)	"*equilibration time*" after swap (days)	Total corrosion time (days)
SA_d, IA_d	*$^{29}SiO_2$, $^{10}B_2O_3$*	*7*	*1*	*8*
SA_e, IA_e	*$^{28}SiO_2$, $^{11}B_2O_3$*	*7*	*1*	*8*
SD_d, ID_d	*$^{29}SiO_2$, $^{10}B_2O_3$*	*29*	*1*	*30*
SD_e, ID_e	*$^{28}SiO_2$, $^{11}B_2O_3$*	*29*	*1*	*30*
SF_d, IF_d	*$^{29}SiO_2$, $^{10}B_2O_3$*	*179*	*1*	*180*
SF_e, IF_e	*$^{28}SiO_2$, $^{11}B_2O_3$*	*179*	*1*	*180*
SB_d, IB_d	$^{29}SiO_2$, $^{10}B_2O_3$	7	7	14
SB_e, IB_e	$^{28}SiO_2$, $^{11}B_2O_3$	7	7	14
SC_d, IC_d	$^{29}SiO_2$, $^{10}B_2O_3$	15	15	30
SC_e, IC_e	$^{28}SiO_2$, $^{11}B_2O_3$	15	15	30
SE_d, IE_d	$^{29}SiO_2$, $^{10}B_2O_3$	75	75	150
SE_e, IE_e	$^{28}SiO_2$, $^{11}B_2O_3$	75	75	150

2.3.3 Saturated Glass Solutions- SGS

Glass powders were digested in 500 mL or 1000 mL PFA jars (Savillex®). The goal of the initial SGS experiments was to determine the amount of starting material needed to completely saturate the glass solutions, and to estimate the saturation concentration for the various SGSs. Several experiments were initially conducted with large amounts of starting glass powder (≥ 75 g) in order to confirm the formation of crystalline material during the dissolution of the simple glasses. Crystalline material formation had been previously observed for LDS systems containing less than 75 g, so it was concluded that this amount of glass would be enough to facilitate a completely saturated LDS SGS. Interestingly, the exact amount of glass powder needed to saturate the solution was not clearly observed for NDS, and for this reason, additional NDS experiments were conducted with different mass/volume (i.e., $M_{glass}/V_{solution}$) ratios.

Based on the results of initial GWB simulations, another series of experiments was initiated with LDS glass to achieve the two following goals: (1) determine the maximum M/V ratio for LDS that would result in total dissolution of the glass powder (viz., no original starting powder is clearly observed in the digestion vessel after some period of time), and (2) benchmark the accuracy of the thermodynamic modeling using different M/V ratios at or near the $(M/V)_{max}$ value. Two experiments using 3.5 g and 5.5 g of LDS powder with a highly varying particle size distribution (hundreds of nanometers to millimeter sized particles) were initialized to straddle the maximum amount of glass dissolved (~ 4 g) that was observed in previous experiments. This maximum mass was determined by calculating the amount of glass in solution in the 75 g LDS experiment based on the highest measured concentration of Si and Li in the SGS. After some time, it was observed that some of the larger particles of glass were not dissolving, and a second set of experiments was started with 5 g and 15 g of finely crushed powder. The digestion vessels were periodically agitated (i.e. shaken) for the first 24 hours of dissolution. A third set of experiments with starting masses of 2.5 g, 7.5 g, and 12.5 g was also undertaken using the same particle size powder as the 5 g and 15 g, and these experiments were also agitated for the first 24 hours of the experiment. While an attempt was made to be consistent with the amount of agitation each vessel underwent, variations in the amount of agitation of each vessel may have led to contrasts in the amount of glass powder that was exposed to solution in each container.

Al contamination was observed in both the NDS and LDS systems. It was later found to be a result of contamination transferred from the refractory "setter" material used during the annealing process for both types of glass. This provided an interesting variable to test in the thermodynamic solution modeling (see Section 2.5). Therefore, another set of experiments was conducted with Al contamination intentionally added to the leaching solution in the form of $Al(OH)_3$ to give 100 ppm Al in solution. The glasses were allowed to react for the first hour in order to drive the pH of the SGS to a level where the $Al(OH)_3$ would become soluble since it is otherwise insoluble in near-neutral pH solutions. It was already known that the pH of the SGS would be close to its equilibrium value within one hour of the experiment's beginning and that these values (~ pH 12-13) would be sufficient to dissolve the small amount of added $Al(OH)_3$.

Table III summarizes all the SGS experiments that were conducted.

Table III. Summary of SGS experiments used for the investigation of solution saturation effects for the simple binary glasses LDS and NDS.

	Glass	M_{glass} (g)	$V_{solution}$ (mL)	Solution
Initial Experiments	**LDS**	75	500	ASTM TYPE I
	NDS	75	500	ASTM TYPE I
	NDS	125	250	ASTM TYPE I
First Titrations*	**LDS**	3.5	500	ASTM TYPE I
	LDS	5.5	500	ASTM TYPE I
Second Titrations	**LDS**	2.5	500	ASTM TYPE I
	LDS	5	500	ASTM TYPE I
	LDS	7.5	500	ASTM TYPE I
	LDS	12.5	500	ASTM TYPE I
	LDS	15	500	ASTM TYPE I
Al Effects Experiments	**LDS w/ 100 ppm Al**	150	1000	ASTM TYPE I
	NDS w/ 100 ppm Al	150	1000	ASTM TYPE I
Precip Exp.	**LDS**	20	60/440	ASTM TYPE I

Approximately 20 mL aliquots of each solution were collected at regular intervals for each of the experiments in Table 1 and refrigerated for subsequent pH and concentration measurements. In order to maintain a constant volume of solution in the digestion vessel, an amount of ASTM Type I water equivalent to the aliquot volume removed was added back to the digestion vessels after each sample aliquot was collected. It was assumed that the solutions' equilibration would not be drastically affected by the removal of a small amount of saturated solution or by replacing this removed amount of SGS with fresh ASTM Type I water. The aliquots were separated into two containers, one for pH analysis and the other for solution concentration measurements via ICP-AES. Samples of the undissolved glass and any precipitated material were also periodically collected and dried for examination with FESEM, EDS, and XRD.

2.4. Characterization of Surface Layer Structure and Evolution

2.4.1. Glass Composition Effects on Structure by NMR

The bulk structure characteristics observed by Bloch decay NMR is similar for most of the glasses studied in this work, independent of the composition. Based on the results of ^{29}Si MAS NMR Bloch decay experiments, the glass networks are comprised of quaternary (Q) $^{[IV]}$Si units, as expected (Figure 3). More specific Q-site speciation and quantification cannot be accomplished for these samples as next-nearest neighbor Al and B cause an overlapping of the Si-Al and Si-B chemical shift ranges.[47,48] Al has primarily tetrahedral coordination as measured by Bloch decay ^{27}Al MAS NMR (Figure 4). This is the preferential form of aluminum, provided enough network modifying cations are present for charge compensation. In glasses with high aluminum content, aluminum can also adopt octahedral coordination. $^{[VI]}$Al is detected via a resonance at 0 ppm. There is little change in the ratio of $^{[IV]}$Al to $^{[VI]}$Al after the various corrosion times since a majority of the signal is derived from the pristine glass. In general, the charge-compensating cations such as sodium and lithium have one resonance that is representative of many environments with different numbers of coordinating oxygens (Figures 5 and 6). Boron is a network forming species and adopts two coordination environments in the pristine glass: trigonal (~18.0 ppm) and tetrahedral (~2.8 ppm) (Figure 7). $^{[III]}$B is a stable form in the glass, but the large amount of network modifying cations facilitates an increase in coordination. Variation in the $^{[III]}$B/$^{[IV]}$B ratio as a function of glass composition is related to differences in the relative proportion of network-modifying cations, which are required to stabilize the negatively charged $[BO_4]^-$ unit (Table III). A simple depiction of a generalized glass structure, based on the information gathered by these measurements, is presented in Figure 8.

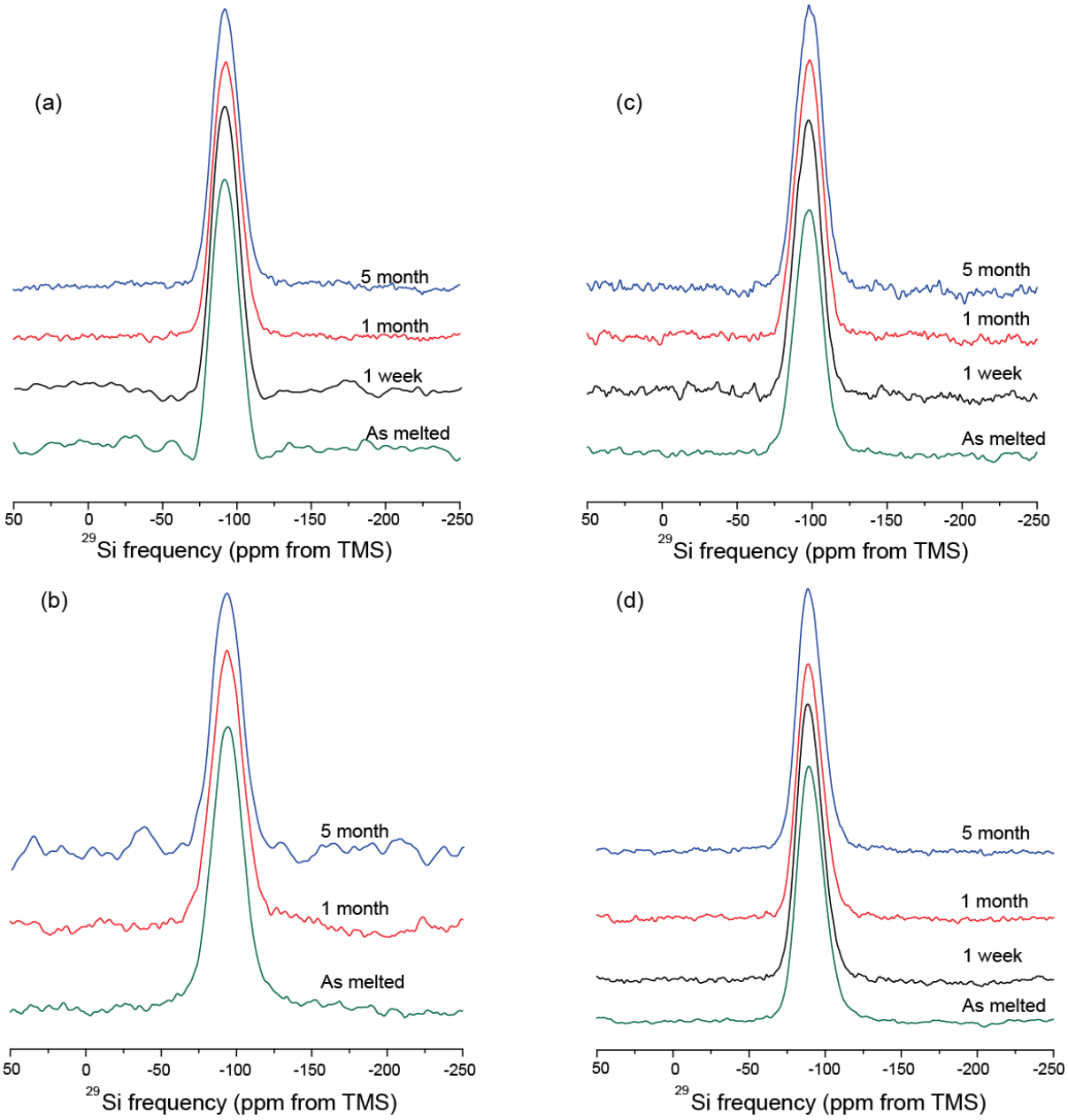

Figure 3. ^{29}Si MAS NMR spectra of (a) SA1R, (b) AFCI, (c) ISG, and (d) SS2R. All samples were analyzed at 9.4 T and spun between 10-11 kHz. Spectra of the same composition with different exposure times have been normalized to remove variation from the number of scans and sample mass.

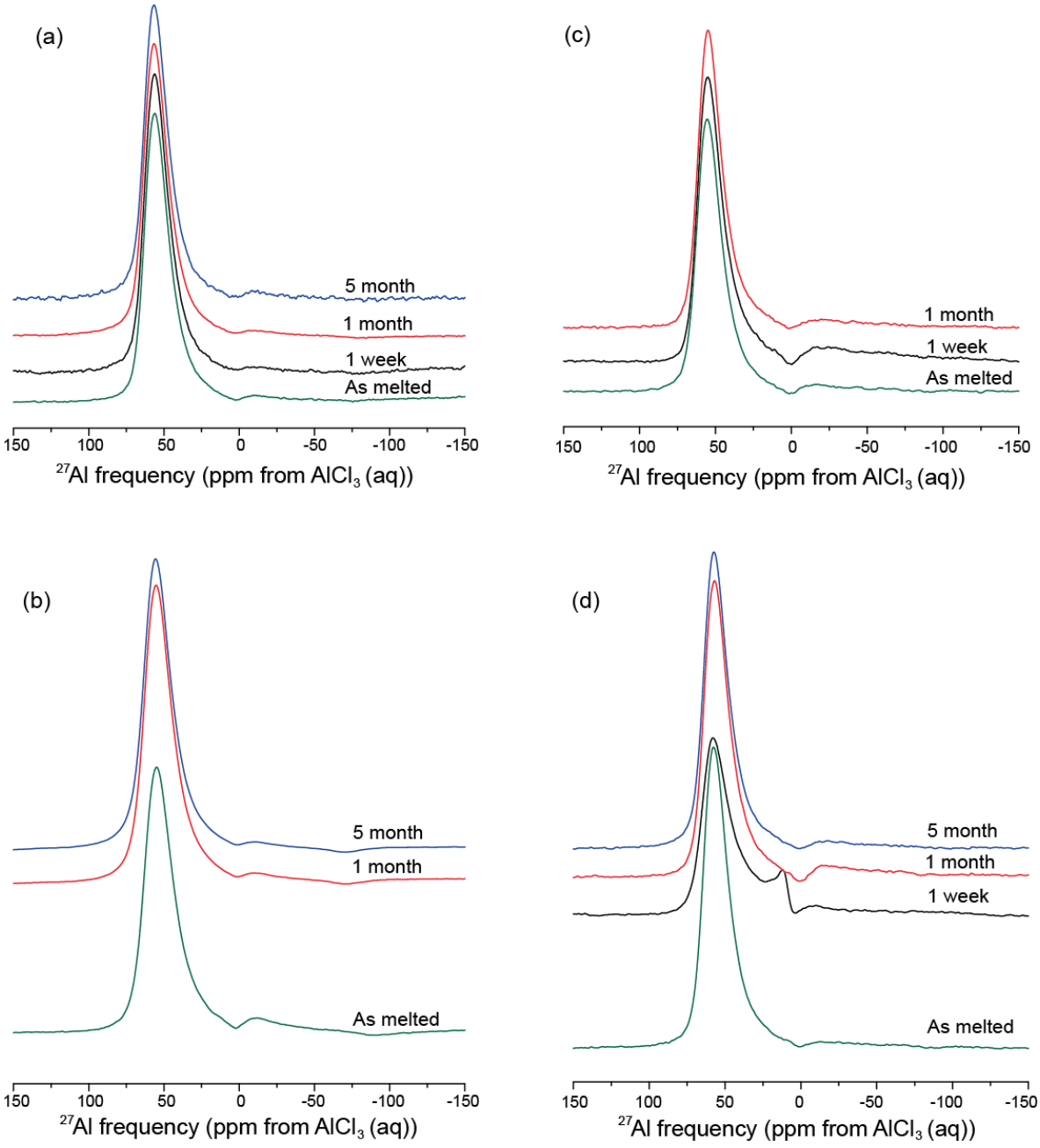

Figure 4. ^{27}Al MAS NMR spectra of (a) SA1R, (b) AFCI, (c) ISG, and (d) SS2R. All samples were analyzed at 11.7 T and spun at 18 kHz. Spectra of the same composition with different exposure times have been normalized to remove variation from the number of scans and sample mass.

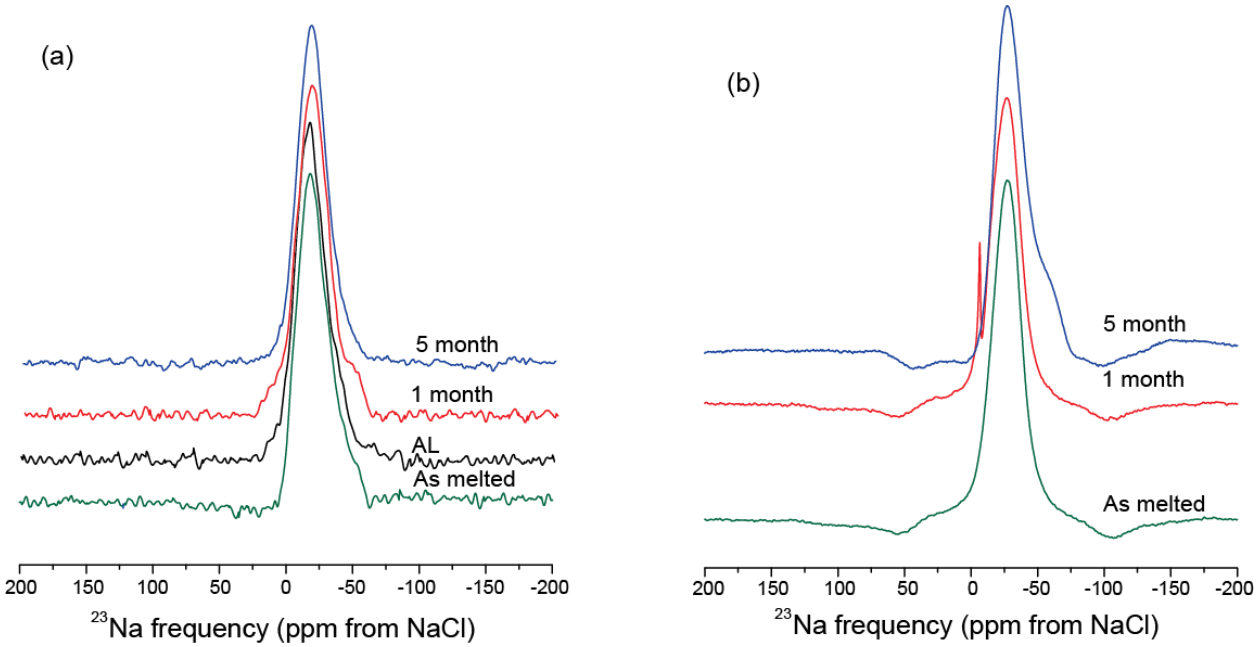

Figure 5. ^{23}Na MAS NMR spectra of (a) SA1R and (b) AFCI. SA1R samples were analyzed at 11.7 T with a spinning speed of 17 kHz. AFCI samples were analyzed at 17.6 T and spun at 18 kHz. Spectra of the same composition with different exposure times have been normalized to remove variation from the number of scans and sample mass.

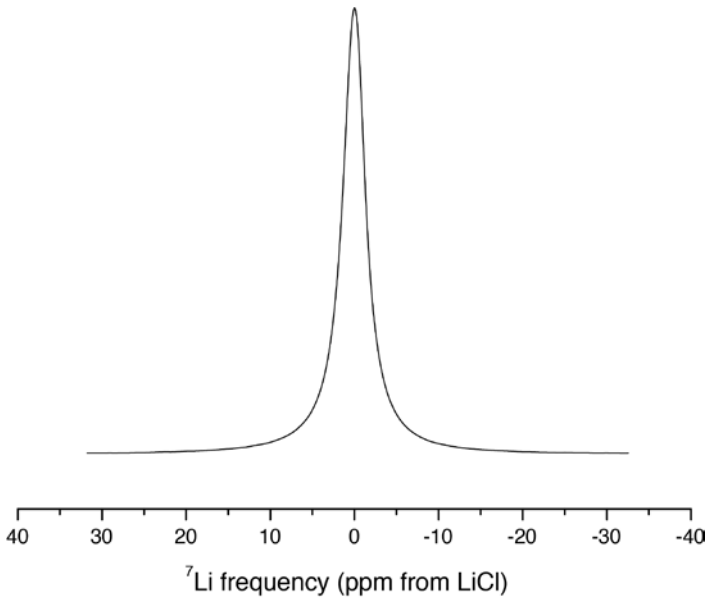

Figure 6. Representative ^{7}Li MAS NMR spectrum on SA1R glass. This sample was analyzed at 9.4 T with a spinning speed of 10 kHz.

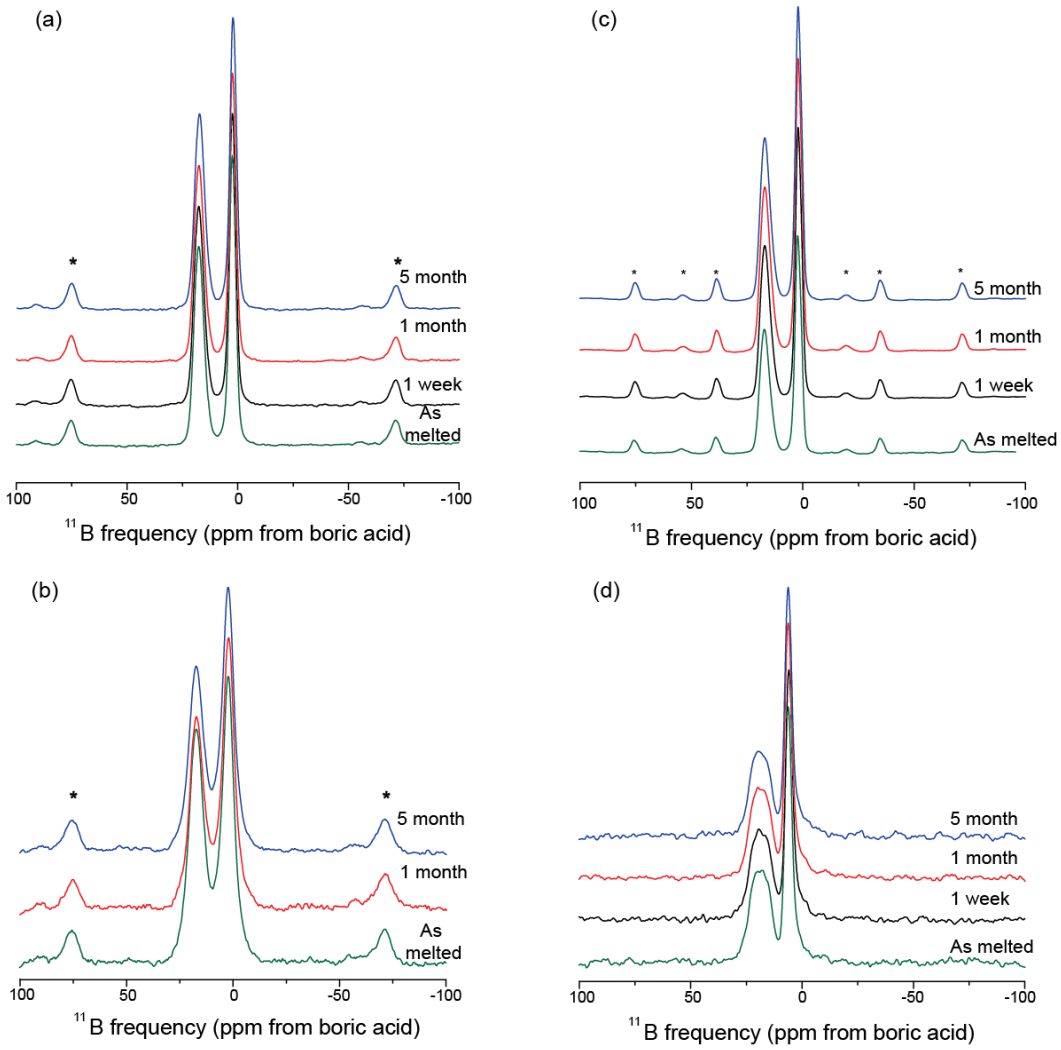

Figure 7. ^{11}B MAS NMR spectra of (a) SA1R, (b) AFCI, (c) ISG, and (d) SS2R. Samples a-c were analyzed at 19.96 T with a spinning speed of 18 kHz. Samples d were analyzed at 11.7 T and spun at 18 kHz. Spectra of the same composition with different exposure times have been normalized to remove variation from the number of scans and sample mass.

Table IV. $^{[III]}B/^{[IV]}B$ Ratios for SA1R, AFCI, ISG, and SS2R after various corrosion times.

Corrosion times	SA1R	AFCI	ISG	SS2R
Pristine, as melted	0.92	0.93	0.85	0.84
1 week	---	---	0.81	0.86
1 month	1.0	0.76	0.84	0.77
5 month	0.91	0.78	0.81	0.74

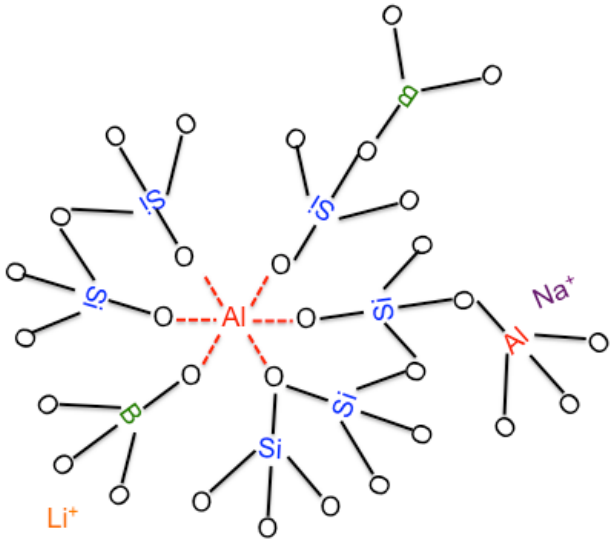

Figure 8. Schematic structure for the glasses studied. Al is both a network specie and modifier.

Although the gel layers of all natural isotopic abundance (NA) compositions studied in this work are composed largely of silica, there are significant differences in the alteration layers as a function of glass composition. One of the primary sources of variation is the relative thickness of the layers formed. The ISG glass has thicker alteration layers than AFCI, SA1R, and SS2R based on our ability to obtain ^{1}H-^{29}Si CP-MAS NMR data without the additional enhancement provided by the CPMG pulse train (Figure 9). Moreover, separate Q species could be identified for ISG while the presence of Al and/or B as a next-nearest neighbor in the other compositions is obscured by resonance overlaps. The detection of $^{[VI]}$Al via ^{1}H-^{27}Al CP-MAS NMR denotes the incorporation of aluminum in the gel layer (Section 2.4.3), which is observed for SA1R, AFCI, and SS2R, but is absent from the ISG spectrum (Figure 10). ^{1}H-^{11}B CP-MAS signal derived from the hydrated glass layer is observed for all compositions and does not differ significantly as a function of composition (Figure 11). In general, the variations observed in the data are attributed to the gel layer. (This is based on the fact that the hydrated glass layer is expected to yield spectra reminiscent of the bulk glass structures which are not significantly different.) This conclusion is supported by the isotopic swapping experiments (see Section 2.4.3 and 2.4.4) which show differences in the gel layer dynamics for different bulk glass compositions. A schematic structure model for the alteration layers of SA1R and AFCI is presented in Figure 12, and a summary of the coordination environments/species found in the alteration layers of all the glasses is provided in Table V.

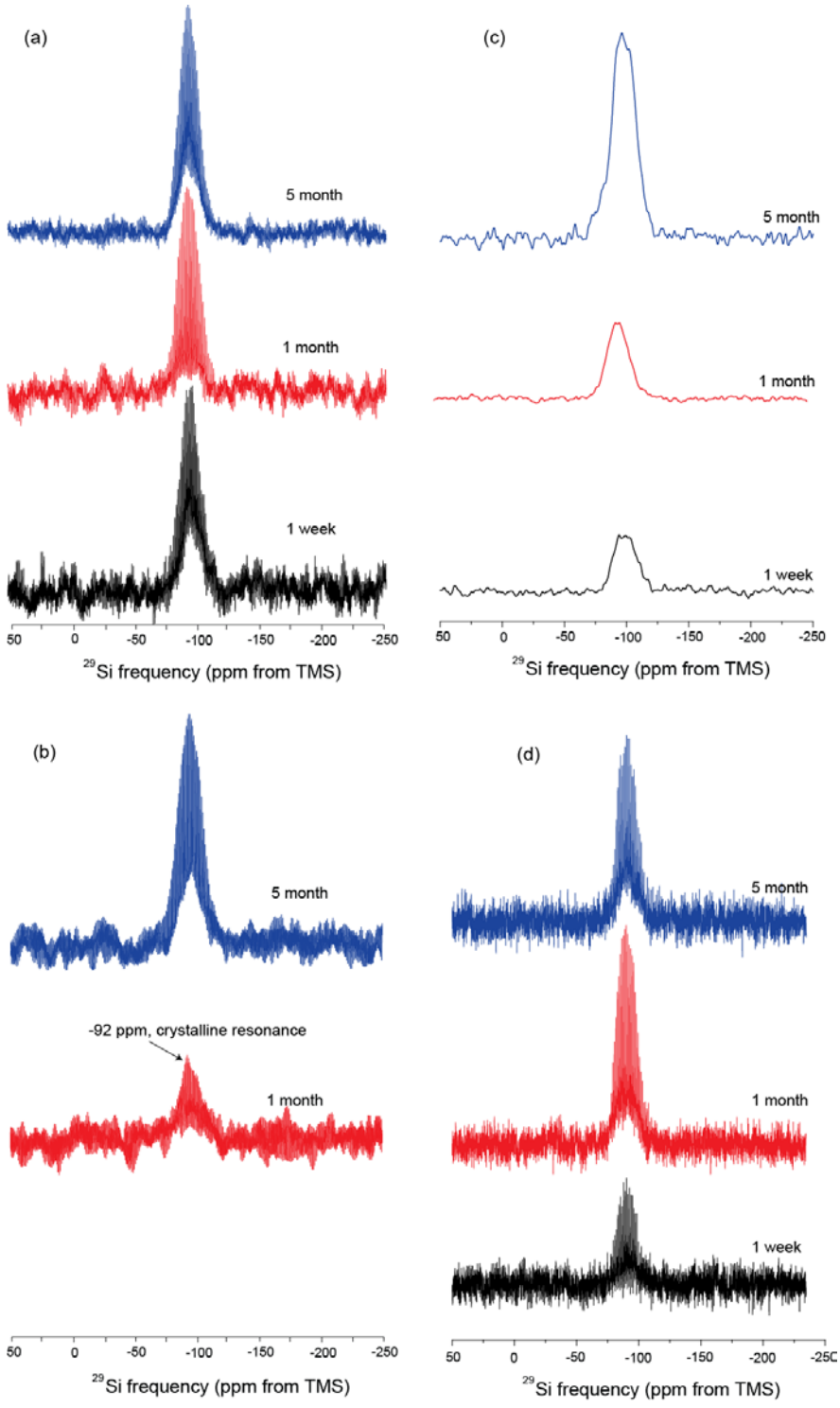

Figure 9. ^{1}H-^{29}Si CP-CPMG MAS NMR spectra of (a) SA1R, (b) AFCI, and (d) SS2R. Samples were analyzed at either 14.1or 19.96 T with spinning speeds between 5-10 kHz. (c) ^{1}H-^{29}Si CP-MAS NMR spectra of ISG glasses with various corrosion regimes. ISG samples were analyzed at 7.1 T with a spinning speed of 5 kHz. Spectra of the same composition with different exposure times have been normalized to remove variation from the number of scans and sample mass.

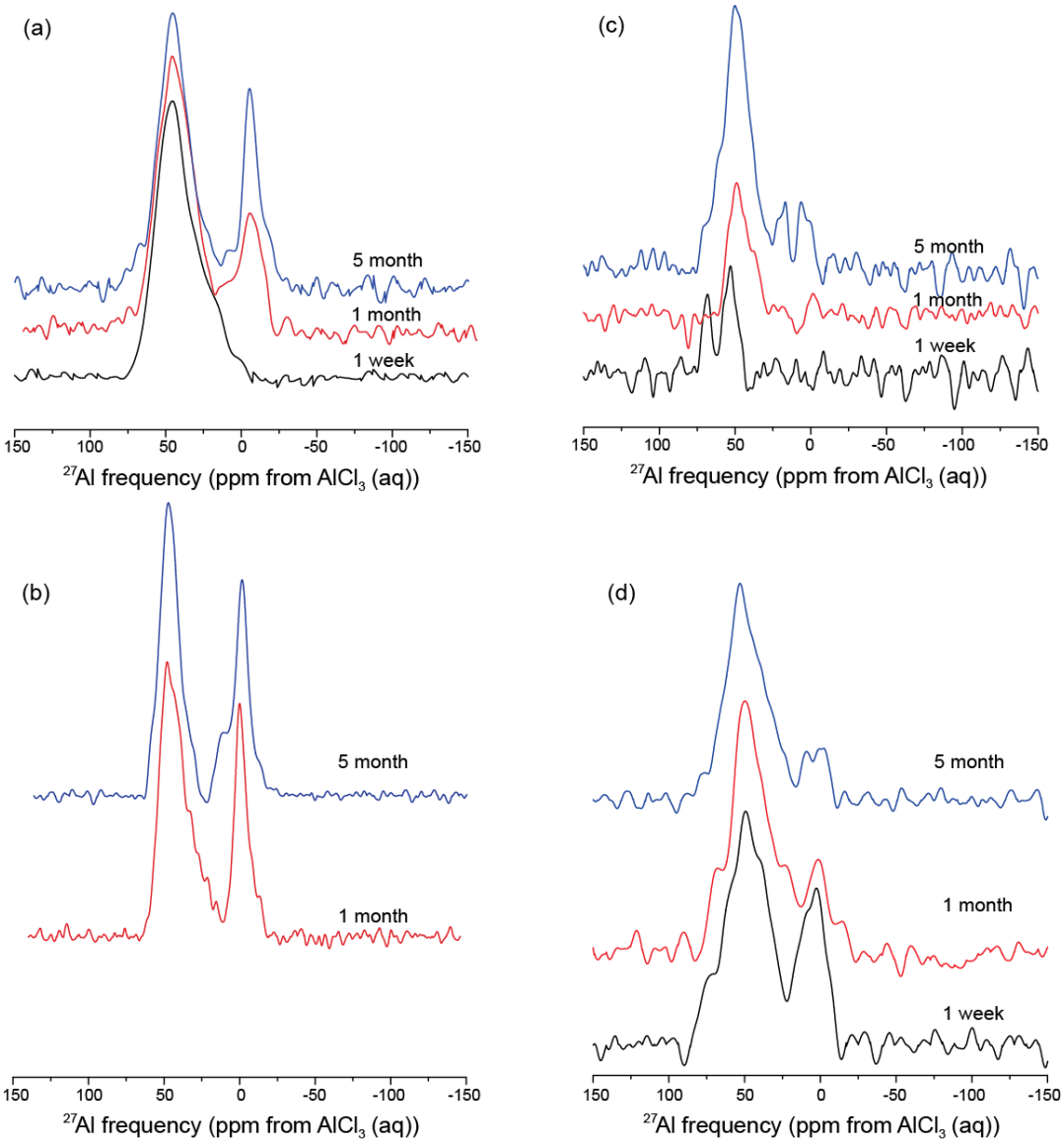

Figure 10. ^{1}H-^{27}Al CP-MAS NMR spectra of (a) SA1R, (b) AFCI, (c) ISG, and (d) SS2R glasses. Samples a, c, and d were analyzed at 7.1 T with spinning speeds of 10 kHz. AFCI samples were analyzed at 18.79 T with a spinning speed of 8 kHz. Spectra of the same composition with different exposure times have been normalized to remove variation from the number of scans and sample mass.

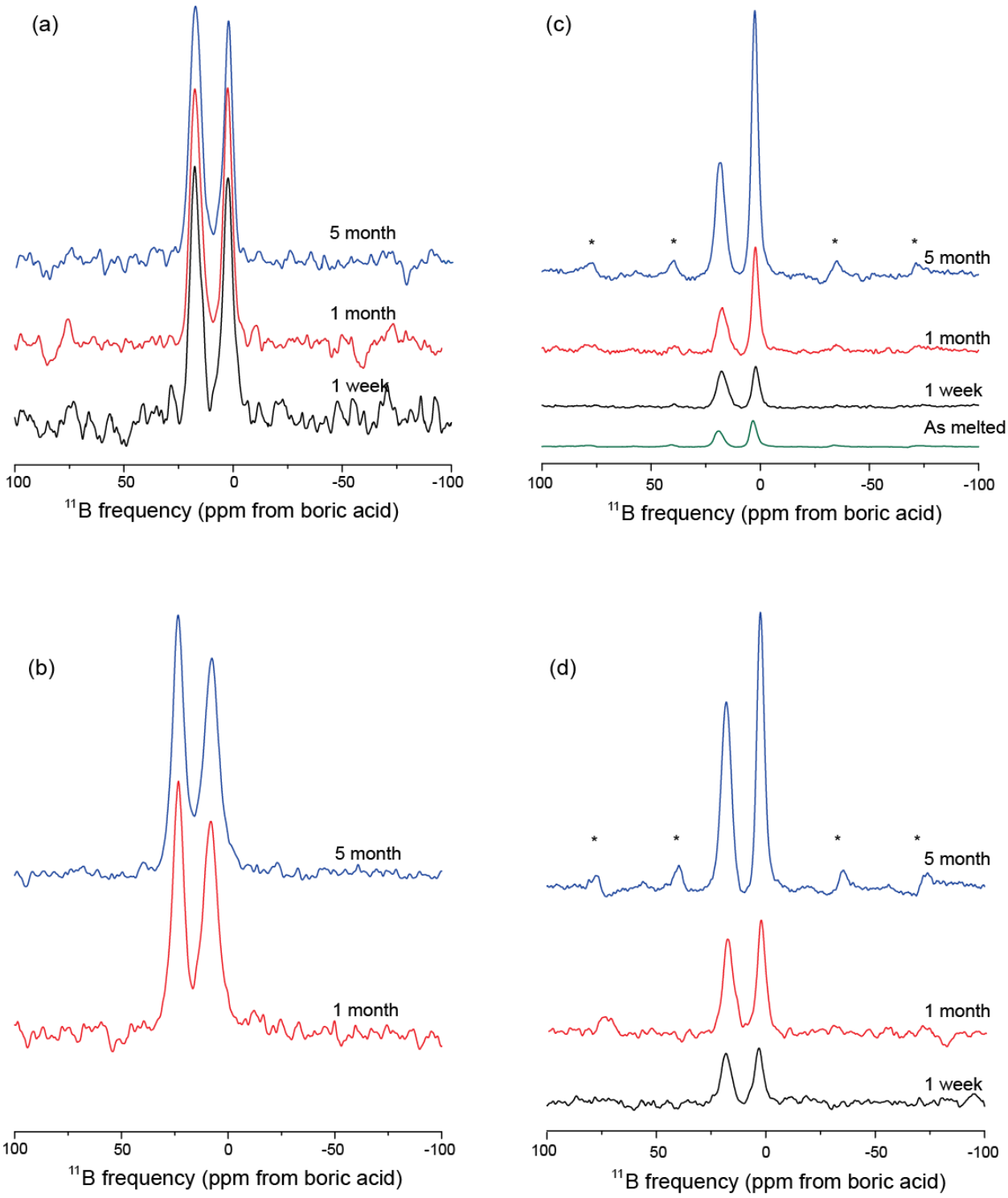

Figure 11. ^{1}H-^{11}B CP-MAS NMR spectra of (a) SA1R, (b) AFCI, (c) ISG, and (d) SS2R glasses. All samples were analyzed at 19.96 T with spinning speeds of either 8 or 20 kHz. Spectra of the same composition with different exposure times have been normalized to remove variation from the number of scans and sample mass.

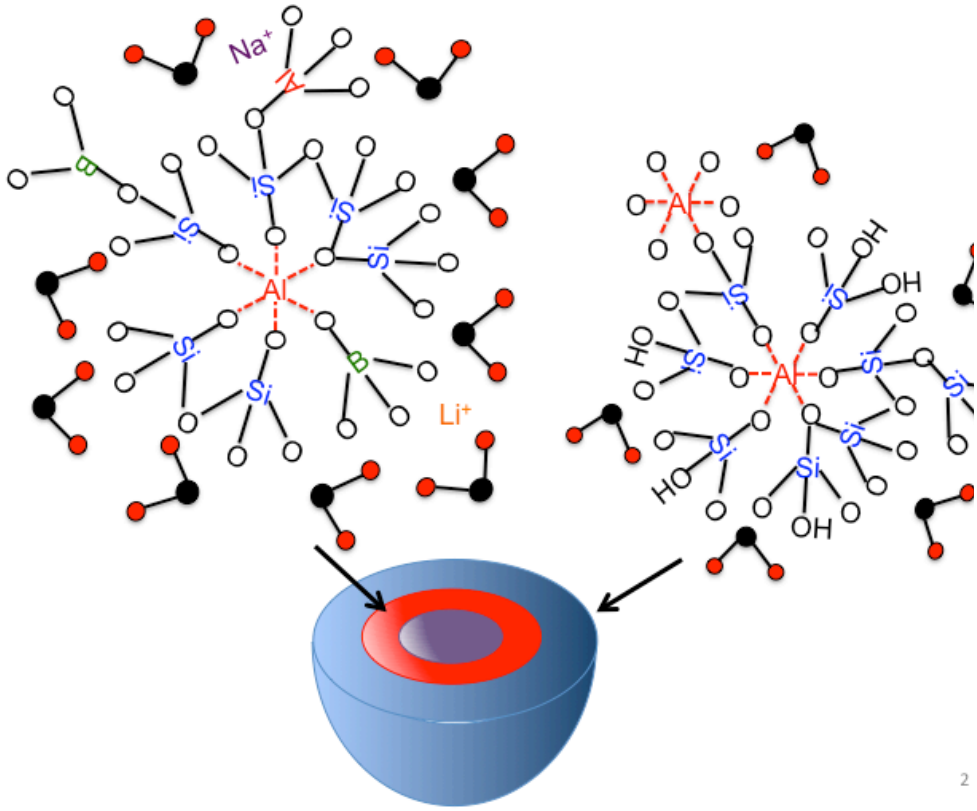

Figure 12. Summary of the structure of alteration layers for AFCI and SA1R glasses. Red, dashed lines indicate coordination of these species, but not direct network bonds

Table V. Summary of Composition Influence on Glass Structure by NMR; the hydrated glass layer is represented as HGL and the gel layer is abbreviated as GL in the table.

Glass Composition	Si in alteration layers	Al in alteration layers	B in alteration layers	Na in alteration layers
AFCI	HGL- $^{[IV]}$Si GL- $^{[IV]}$Si, crystalline phases	HGL- $^{[IV]}$Al GL- $^{[VI]}$Al	HGL- $^{[III]}$B, $^{[IV]}$B GL- absent	HGL- many environments GL-absent
SA1R	HGL- $^{[IV]}$Si GL- $^{[IV]}$Si	HGL- $^{[IV]}$Al GL- $^{[VI]}$Al	HGL- $^{[III]}$B, $^{[IV]}$B GL- absent	HGL- many environments GL-absent
ISG	HGL- $^{[IV]}$Si GL- $^{[IV]}$Si (Thick layers)	HGL- $^{[IV]}$Al GL- absent	HGL- $^{[III]}$B, $^{[IV]}$B GL- absent	Not measured
SS2R	HGL- $^{[IV]}$Si GL- $^{[IV]}$Si	HGL- $^{[IV]}$Al GL- $^{[VI]}$Al (sparingly)	HGL- $^{[III]}$B, $^{[IV]}$B GL- absent	Not measured

2.4.2. Fiber versus Powder Corrosion

Fibers were used in this study because, in contrast to glass powder, they have a reproducible pristine initial surface, and a relatively high surface area with uniform geometry and reactivity. Another advantage is the high ratio of "altered layer" volume to "bulk glass" volume which provides a degree of surface sensitivity independent of the analytical technique used to probe the sample. In contrast, the crushing of monolithic pieces of glass to make glass powder for corrosion testing introduces microcracks, sharp reactive edges and stress. Cracks distort the initial/forward reaction kinetics and correspondingly, the solution data. Also, solution trapped inside the cracks can remain static and thereby influence the nature of the reaction front; this is especially problematic under alkaline conditions. It should also be noted that the rate at which glass cools affects the density of the glass, and thereby the reactivity and associated diffusion coefficients for leachable ions. Thus, it is to be expected that fibers will yield an upper limit on the leaching and dissolution kinetics of a glass. And since glass corrosion involves two simultaneous reaction mechanisms, leaching and dissolution, fibers offer a way to monitor each directly and independently. Leaching occurs through ion exchange, causing minimal weight loss and significant surface layer formation which can be measured in various ways. Dissolution is a breakdown of the glass structure, resulting in weight loss and dimensional changes in the material. Since the initial fiber diameters are uniform throughout the sample, a direct measurement of the velocity of these two reaction fronts is possible:

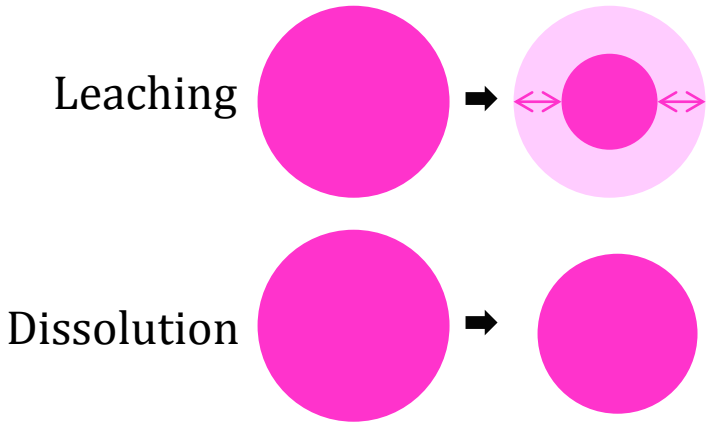

Figure 13. Cross-sectional analysis of leached fibers can be used to obtain both surface layer thickness and recession of the original surface due to total dissolution.

The single-pass flow-through (SPFT) apparatus for corrosion studies is designed to expose the sample to controlled flow conditions to prevent exposure to the products of dissolution; ie, it measures the forward 'upper limit' dissolution rate. Here, it was used to expose SS1R glass fibers and glass powders to controlled leaching conditions (pH 5 and pH 8 at two different flow rates) for analysis of the altered layers. Solution analysis was also performed to obtain the forward dissolution rate (although that was not the main objective of the experiments). A primary objective was to obtain "bulk alteration layer" by leaching the fibers throughout their cross-section; this objective was achieved but insufficient time was available to use those "bulk gels" for NMR. Another objective was to expose fresh glass fiber to solutions representative of the saturated glass solution occluded within the altered layer at long times; viz, to simulate the pristine glass/altered layer interface; this objective has not yet been achieved

Figures 14 and 15 show the solution analysis data for the fiber versus powder experiments, while figures fibers and powders show evolution of the materials after leaching. Several points are worth noting. If the experiment had ideal single-pass flow-through conditions, the pH of the effluent solution should be the same as the pH of the influent solution. The rise in pH to equilibrium 9.8 in all runs demonstrates that ideal dynamic conditions were not reached; the corroding glass changed the environment of the solution. ASTM C1662 6.9.2 suggests there is a lower threshold for simulated dynamic conditions which is dependent on the glass dissolution rate and the surface area in the test. For the samples examined here, solution and affinity effects were likely in play, and must be considered in the interpretation of the results.

It is especially interesting to note that the dissolution rates seem to be approaching a common value independent of the initial pH or the flow rate. Not surprisingly, the rate of approach to that value varies with the flow rate and form of the sample. EDS line-scans across the fiber diameters showed that the fiber leached with a 15 ml/day flow rate had a spike of sodium corresponding to the center of the fiber. The corresponding Na line-scans for the pH 5 and pH 8 60ml/day fibers were at background indicating that these fibers were leached through the cross-section. Initial and final diameters of the fibers were measured by averaging at least 10 diameter measurements taken in the FESEM; the fibers were randomly selected from the two identical sample bottles. The initial distribution of fiber diameters is small, but finite, so there is some error in the measured diameter changes since an average initial value must be assumed. Nevertheless, all of the leached fibers showed an increase in diameter! This increase needs to be validated in another set of tests, but if true, it may be due to swelling of the fiber because of water swelling the porous altered layer. It could also be due to mass transport from the inside of the fiber to the outside, possibly causing the holes found at the central axis of all the leached through 60 ml/day fibers as shown in the FESEM of Figure 16.

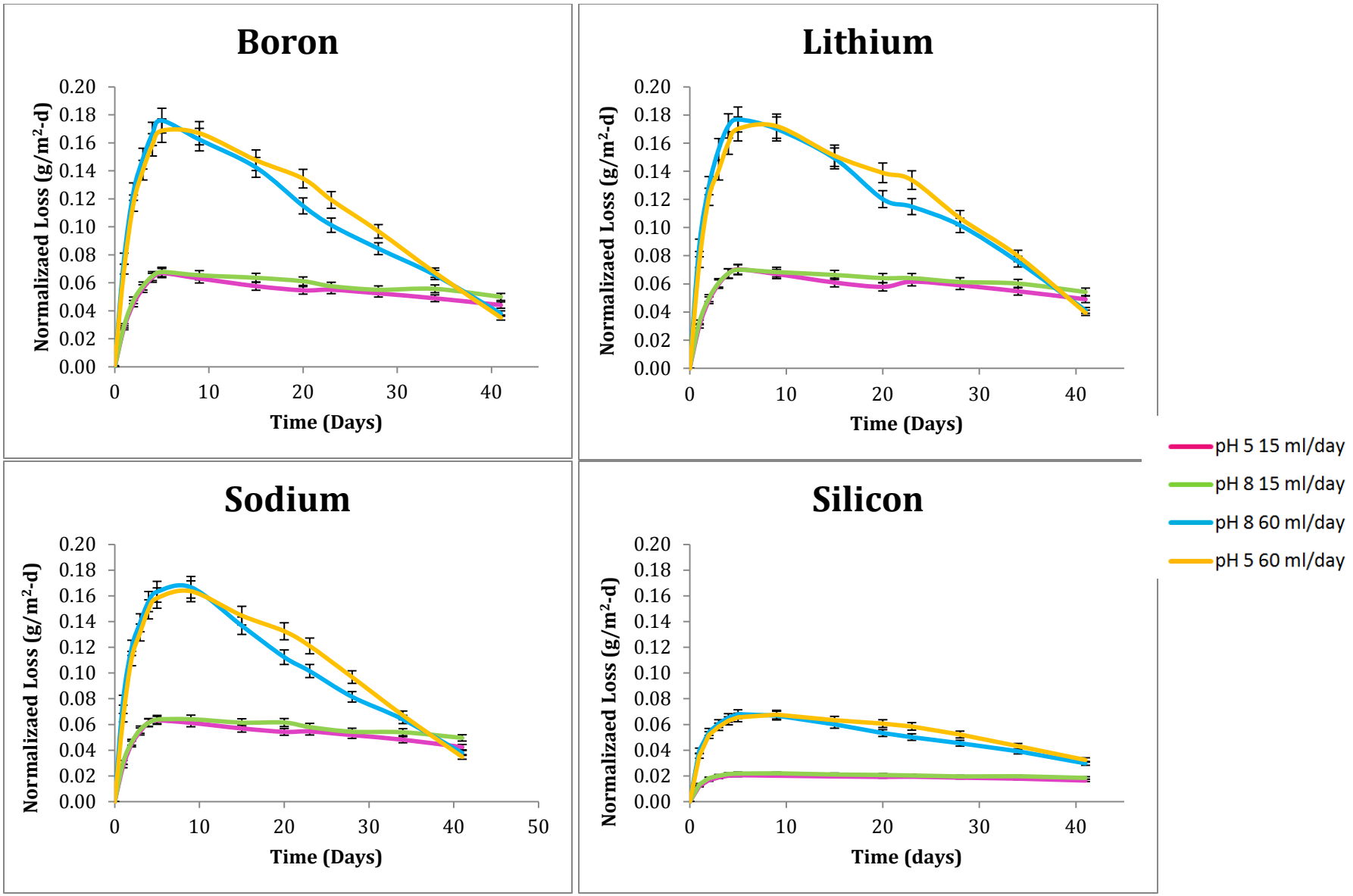

Figure 14. ICP-AES results for boron, lithium, sodium, and silicon from SS1R glass fiber.

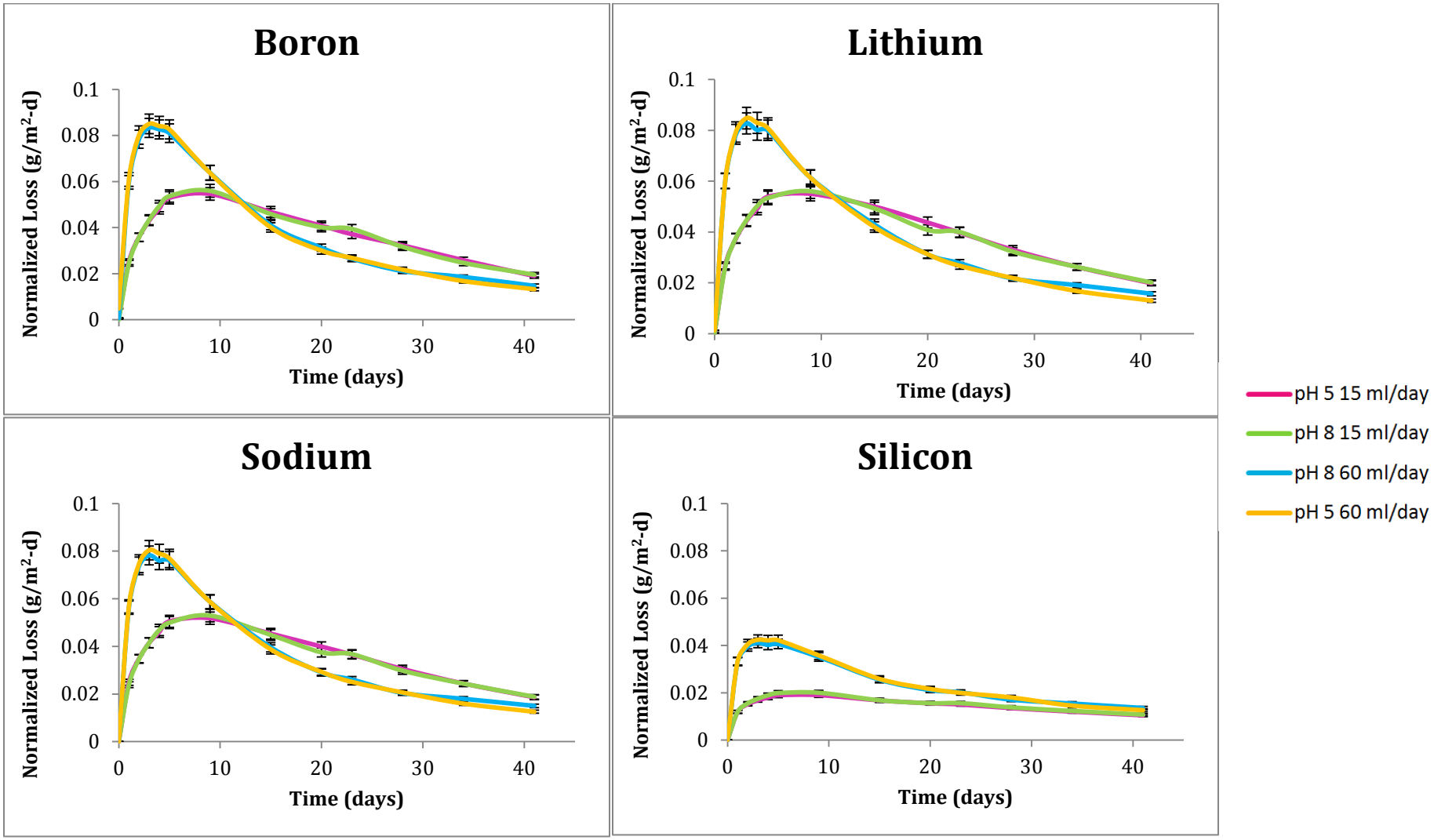

Figure 15. ICP-AES results for boron, lithium, sodium, and silicon from SS1R glass powder.

(a) 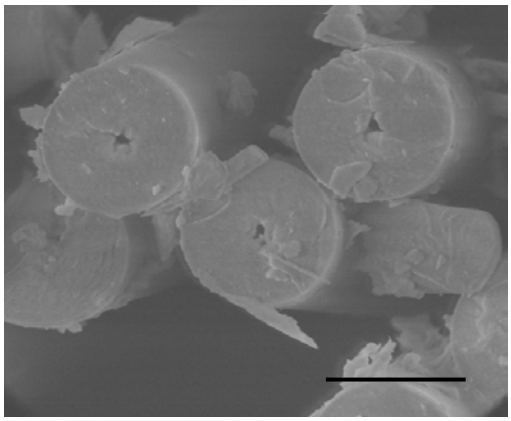 (b) 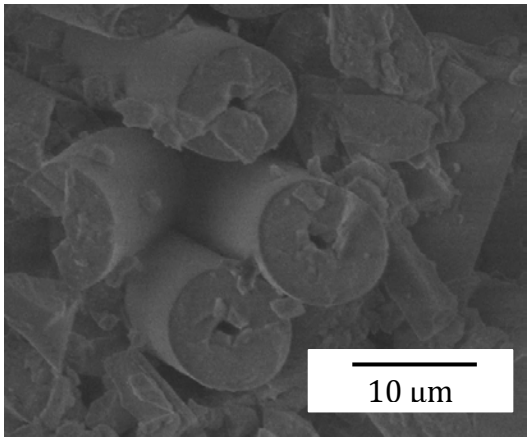

Figure 16. FESEM images of SS1R fiber with a solution flow rate of 60 mL/day and initial pH values of (a) 5 and (b) 8.

To further evaluate the extent of "total leaching" of B, Na and other leachable modifiers, a calculation of the extent of leaching was performed using the solution analysis data. This was accomplished through integration of the solution analysis data (for B, Na, Li and Si), and comparison to the initial quantity of each of these species in the SPFT containers to yield a "percent extracted". The 60 ml/day fiber showed 80-90% leach percent leaching for the modifiers, supporting the EDS result that the fibers have been leached through completely, whereas the 15 ml/day fiber was leached less than 50%. A comparable set of calculations for the glass powder showed no dependence on initial pH or flow rate. Relevant to this, it is interesting to note that the powders showed more leaching at the 15ml/day rate than the fibers. We hypothesize that this is due to the highly reactive edges, cracks and fines on the powders which distort the initial kinetics at these low flow rates; at 60ml/day, this effect is negligible. It is likely that Si solution concentration is playing a significant role here, and this is supported by the solution data which shows the highest Si concentrations for fibers at 15ml/day! Also evident in this data is the Li behavior where a higher degree of leaching is observed than for Na or B in almost all leaching conditions. Altogether, it seems that the study of leaching and dissolution using glass fibers offers additional insight to the mechanisms of leaching and dissolution. Of course, the measured dissolution rates for the fibers are high compared to annealed or slow cooled glass (due to the high cooling rate/fictive temperature of the fibers), but the reaction mechanisms may be revealed by the fact that the 'affinity" effects of fibers and their leachate are nearly identical to those of powders and monoliths, whereas the transport and diffusion effects of ions and water will be very different due to the lower density of the fiber structure.

Unfortunately, the SS1R fibers described above could not be studied with NMR because they contained Fe. For this reason, selected experiments were subsequently performed using SS2R fibers and powder. Of particular note was the contrasting behavior of Al in fiber versus powder as shown in Figure 17. The powder retains aluminum in the surface alteration layers under all exposure times as determined by ^{1}H-^{27}Al CP-MAS NMR. For the fiber, however, Al signal was not detected for the longer exposure times suggesting either no aluminum in the layers or none in close proximity to ^{1}H. Figure 18 presents ^{1}H-^{29}Si CP-MAS NMR for fiber versus powder revealing a very strong signal for the final. This is indicative of a thicker silica gel layer (as observed in Section 2.4.1 for the ISG glass). Finally, it is noted that the bonding environments of boron in the alteration layers differ between the powder and fiber. Figure 19 shows that there is more coupling between ^{1}H-$^{[IV]}B$ than ^{1}H-$^{[III]}B$ in the powder while the opposite is true for the fiber (despite having approximately the same amount of boron in the layers based on signal intensity). Exact percentages of $^{[III]}B$ versus $^{[IV]}B$ in the alteration layers cannot be determined by this technique, but the variation between the powder and fiber. This is consistent with data in the literature showing an increase in the $^{[III]}B$ to $^{[IV]}B$ ratio at high cooling rates. Overall, these data imply that the thermal history of the glass, and its uniformity throughout a casting or sample, can influence the leaching and dissolution behavior.

A summary of the coordination environments and species found in the alteration layers of SS2R powder and fiber are described in Table VI.

Table VI. Summary of powder and fiber alteration layers

Glass Composition	Si in alteration layers	Al in alteration layers	B in alteration layers	Na in alteration layers
SS2R powder	HGL- $^{[IV]}Si$ GL- $^{[IV]}Si$	HGL- $^{[IV]}Al$ GL- $^{[VI]}Al$ (sparingly)	HGL- $^{[III]}B$, $^{[IV]}B$ GL- absent (same amount as fiber)	Not measured
SS2R fiber	HGL- $^{[IV]}Si$ GL- $^{[IV]}Si$ (Thick layers)	HGL- $^{[IV]}Al$ GL- $^{[VI]}Al$ (only at short corrosion times)	HGL- $^{[III]}B$, $^{[IV]}B$ GL- absent (same amount as powder)	Not measured

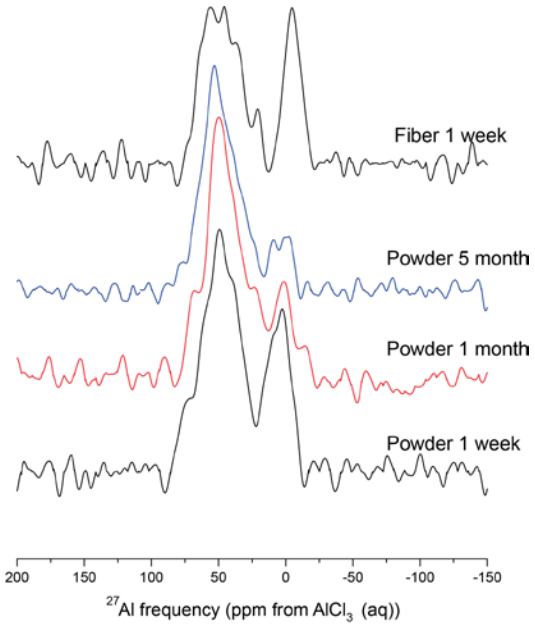

Figure 17. ^{1}H-^{27}Al CP-MAS NMR spectral comparisons of SS2R powder and fiber. All samples were analyzed at 7.1 T with spinning speeds of 10 kHz. Spectra have been normalized to remove variation from the number of scans and sample mass.

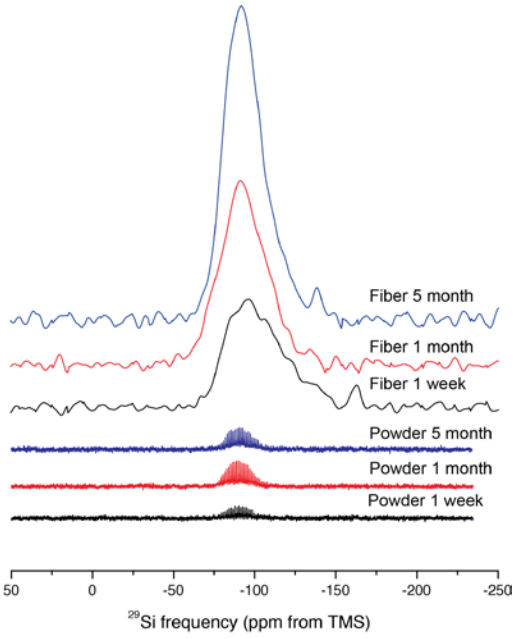

Figure 18. ^{1}H-^{29}Si CP-CPMG MAS NMR spectra of SS2R powder (bottom) and ^{1}H-^{29}Si CP-MAS NMR spectra of SS2R fiber (top). Powder samples were analyzed at 19.96 T with spinning speeds of 8 or 10 kHz. Fiber samples were analyzed at 7.1 T with spinning speeds of 5 kHz. Spectra have been normalized to remove variation from the number of scans and sample mass.

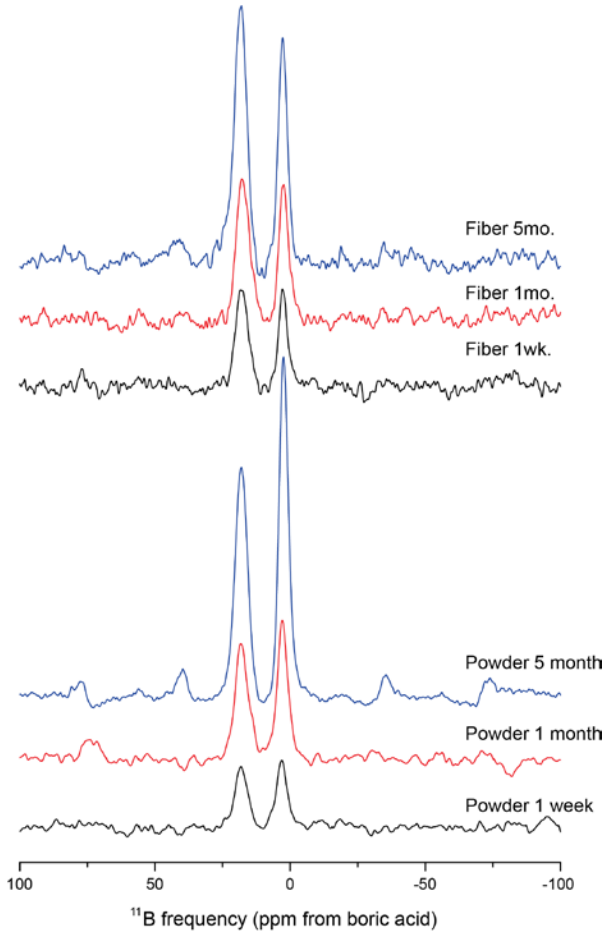

Figure 19. ^{1}H-^{11}B CP-MAS NMR spectra of SS2R fiber (top) and SS2R powder (bottom). Samples were analyzed at 19.96 T with spinning speeds of 10 or 20 kHz. Spectra have been normalized to remove variation from the number of scans and sample mass.

2.4.3. Evolution of Surface Structure by Isotope Exchange

Several different mechanisms have been proposed to explain the formation of alteration layers including network hydrolysis, dissolution/precipitation, and recondensation of solution species.[20,49-58] In this section, the swapping experiments (see Table II) are used to evaluate the dynamics of chemical interaction between the altered surface layer and species in the contacting solution. Of particular interest are the time-dependent structural evolution of the glass surface into a leached hydrated layer and later to a silica gel layer, and the possible nucleation of crystalline phases. The silica gel is expected to age and coarsen over long times, and this too is relevant to both transport and thermodynamic stability. In order to characterize the gel evolution, variation in the Q^n speciation (Figure 20) due to the interaction of ^{29}Si species from solution with the ^{28}Si enriched glass powder, was evaluated. High Q^n species (Q^3 and Q^4) are likely to form during recondensation through the generation of additional bridging oxygen bonds after the adsorption of silicic acid from solution. For SA1R glass, the ability to detect ^{29}Si signal for all $^{28}SiO_2$ enriched samples by both Bloch decay and cross-polarization (Figures 21 and 22) indicates that the interaction between solution silicon and the powder was rapid and occurs during the initial stages of corrosion. Moreover, there was a corresponding increase in the amount of recondensation with equilibration time between the solution and powder. For ISG glass, however, there was no increase in amount of recondensation until equilibration times were much longer (Figures 22 and 23). Variation in the Q^n assignments between Bloch decay and CP-MAS NMR of both compositions results from the fact that CP-MAS NMR is not quantitative and does not have equivalent polarization transfer to all silicon species. The summaries presented in Tables VII-X, albeit qualitative, reveal a time dependent trend towards higher coordination of Si in the gel. This is not surprising, but this work indicates that it is mediated by a rapid and continuous remodeling of the gel through adsorption-desorption and recondensation with Si species in the bulk solution.

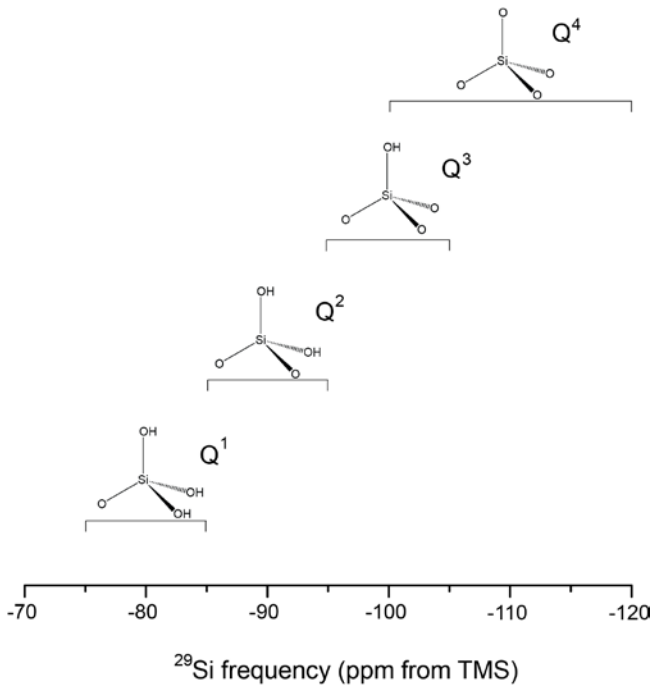

Figure 20. Q^n silicon speciation and associated chemical shift ranges.

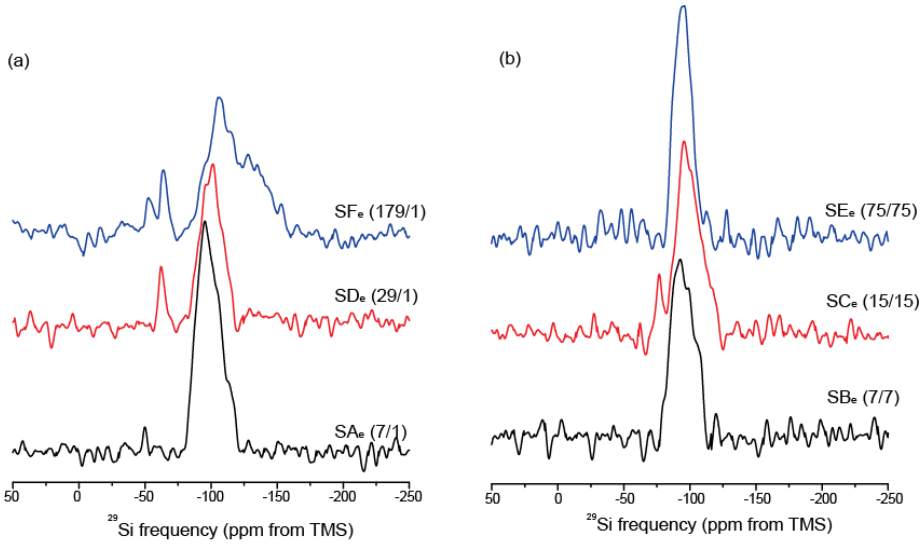

Figure 21. ^{29}Si MAS NMR spectra of SA1R$_e$ glasses enriched in $^{28}SiO_2$. All signal derived from these glasses results from the interaction of ^{29}Si in solution with the $^{28}SiO_2$-enriched powder. Spectra with the same equilibration time have been normalized to remove the influence of variation in the sample mass and number of scans. (a) Samples have 1-day equilibration time and (b) samples have equilibration times equivalent to the initial corrosion time. Samples were analyzed at 9.4 T with spinning speeds of 10 kHz.

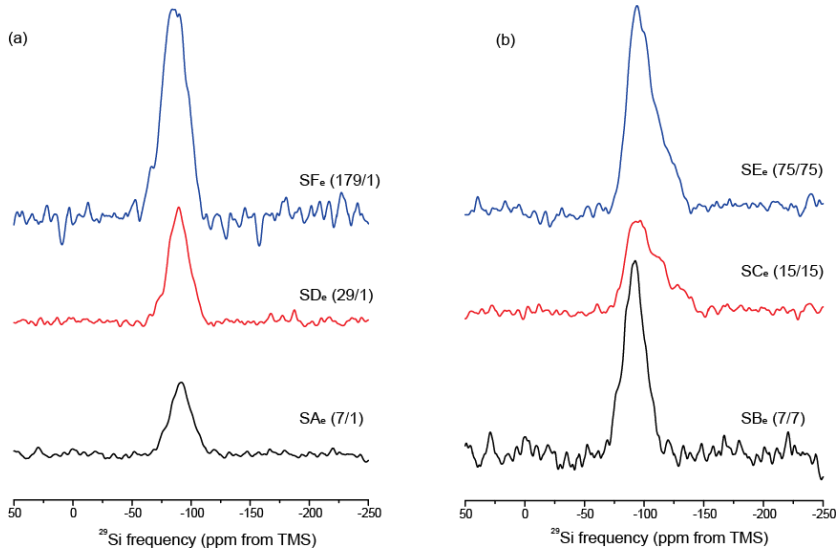

Figure 22. ^{1}H-^{29}Si CP-MAS NMR spectra of SA1R$_e$ glasses enriched in $^{28}SiO_2$. All signal derived from these glasses results from the dipolar interaction of ^{1}H nuclei with ^{29}Si from solution that has reacted with the $^{28}SiO_2$-enriched powder. Spectra have been normalized to remove the influence of variation in the sample mass and number of scans. (a) Samples have a 1-day equilibration period and (b) samples have equivalent initial corrosion and equilibration periods.

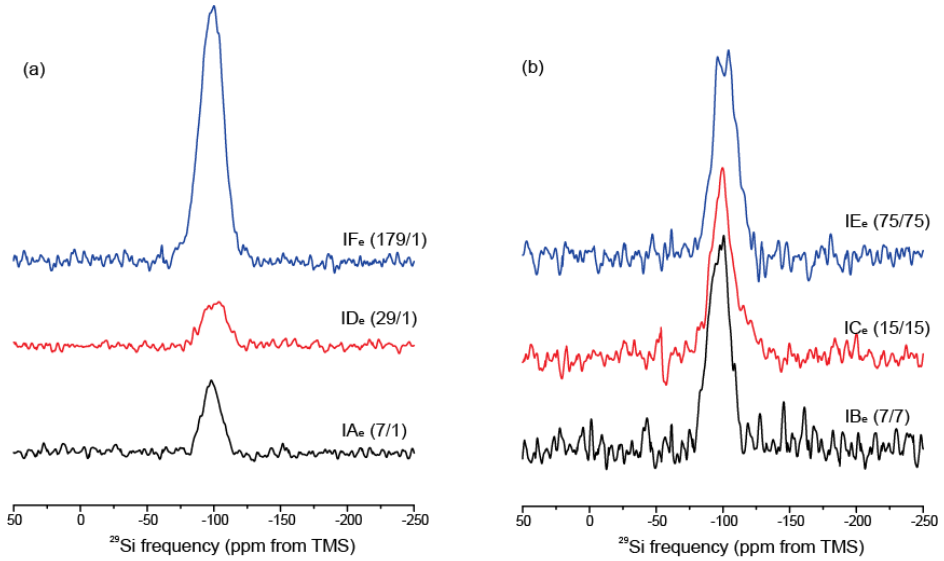

Figure 23. ^{29}Si MAS NMR spectra of ISG_e glasses enriched in $^{28}SiO_2$. All signal derived from these glasses results from the interaction of ^{29}Si in solution with the $^{28}SiO_2$-enriched powder. Spectra with the same equilibration time have been normalized to remove the influence of variation in the sample mass and number of scans. (a) Samples have 1-day equilibration time and (b) samples have equilibration time equivalent to the initial corrosion time.

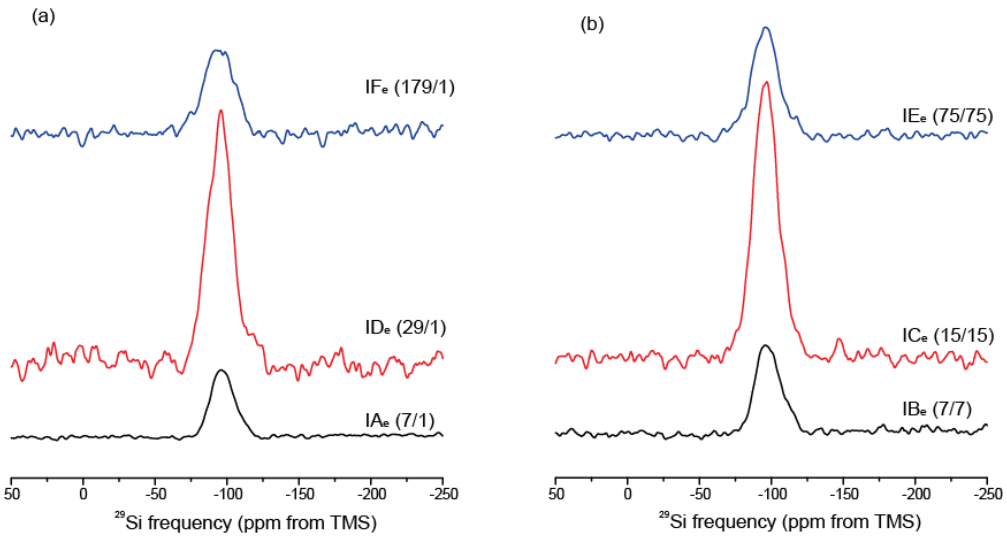

Figure 24. ^{1}H-^{29}Si CP-MAS NMR spectra of ISG_e glasses enriched in $^{28}SiO_2$. All signal derived from these glasses results from the dipolar interaction of ^{1}H nuclei with ^{29}Si from solution that has reacted with the $^{28}SiO_2$-enriched powder. Spectra have been normalized to remove the influence of variation in the sample mass and number of scans. (a) Samples have a 1-day equilibration period and (b) samples have equivalent initial corrosion and equilibration periods.

Table VII. Q^n species observed by ^{29}Si MAS NMR were designated as either low (Q^1 and Q^2) or high (Q^3 and Q^4) for $SA1R_e$ glasses with 1-day equilibration time (italics) and equivalent equilibration time (normal text). Quantification was completed by deconvolution with NUTS NMR processing software (Acorn, Inc.).

Sample	Low Q^n species (%)	High Q^n species (%)
SA_e	*56.7*	*43.2*
SD_e	*45.2*	*54.7*
SF_e	*13.2*	*71.5*
SB_e	72.1	27.9
SC_e	5.4	94.6
SE_e	50.9	49.1

Table VIII. Q^n species observed by ^1H-^{29}Si CP-MAS NMR were designated as either low (Q^1 and Q^2) or high (Q^3 and Q^4) for $SA1R_e$ glasses with 1-day equilibration time (italics) and equivalent equilibration time (normal text). The relative proportion of Q^n species cannot be absolutely quantified, but comparisons between samples can be made.

Sample	Low Q^n species (%)	High Q^n species (%)
SA_e	*81.1*	*18.9*
SD_e	*87.5*	*12.5*
SF_e	*99.5*	*0.5*
SB_e	77.6	22.4
SC_e	38.8	61.2
SE_e	47.5	52.5

Table IX. Q^n species observed by ^{29}Si MAS NMR were designated as either low (Q^1 and Q^2) or high (Q^3 and Q^4) for ISG_e glasses with 1-day equilibration time (italics) and equivalent equilibration time (normal text). Quantification was completed by deconvolution with NUTS NMR processing software (Acorn, Inc.).

Sample	Low Q^n species (%)	High Q^n species (%)
IA_e	*36.4*	*63.6*
ID_e	*24.6*	*74.2*
IF_e	*32.0*	*68.0*
IB_e	49.1	50.9
IC_e	17.1	82.9
IE_e	8.9	91.1

Table X. Q^n species observed by ^1H-^{29}Si CP-MAS NMR were designated as either low (Q^1 and Q^2) or high (Q^3 and Q^4) for ISG_e glasses with 1-day equilibration time (italics) and equivalent equilibration time (normal text). The relative proportion of Q^n species cannot be absolutely quantified, but comparisons between samples can be made.

Sample	Low Q^n species (%)	High Q^n species (%)
IA_e	*0*	*100*
ID_e	*32.4*	*67.6*
IF_e	*68.5*	*31.5*
IB_e	45.2	54.8
IC_e	55.0	45.0
IE_e	38.6	61.4

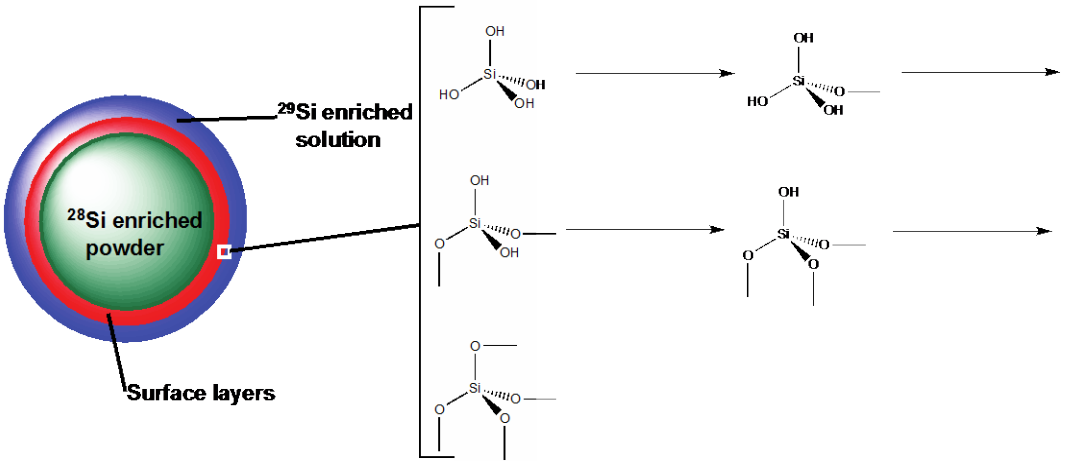

Figure 25: Depiction of the recondensation, where consecutive bonds form between aqueous silicic acid and the gel layer of the corroded glass powder.

Figure 25 shows the recondensation reactions that occur during the interaction of soluble silica with the silica gel layer, but other reactions are likely involved in the gel layer evolution. The detection of signal for ^1H-^{11}B CP-MAS NMR in all samples (Figure 11), and ^1H-^{23}Na CP-MAS NMR in AFCI and SA1R-NA samples (Figure 26), supports a direct effect of hydrolysis in the initial release of Na and B at the pristine glass/gel-layer interface. In the experiments on SA1R-NA and AFCI-NA, the incorporation of aluminum into the gel layer was also observed, facilitated by an increase in coordination from $^{[IV]}Al$ to $^{[VI]}Al$. The presence of a weak feature in the $^{[V]}Al$ chemical shift region (~30 ppm) in the SA1R sample spectrum, indicated that penta-coordinate aluminum might acts as an intermediate in the transition of $^{[IV]}Al$ to $^{[VI]}Al$ (Figure 10). The observation of $^{[V]}Al$ is supported by the computational work of Criscenti et al.[59], who suggested a similar mechanism for aluminum coordination increase (see Figure 27). This transition may be an indication of Ostwald ripening, where an unstable intermediary is formed when it has an energy close to the starting phase.[60] Jantzen et al. also proposed the mechanism of Ostwald ripening in the formation of alteration layers in other glass systems. [61] Overall, the increase in coordination is facilitated by hydrolysis of aluminum in the glass network before incorporation into the gel layer. These data indicate that hydrolysis causes changes in the bonding and structural arrangements of certain components to form the alteration layers.

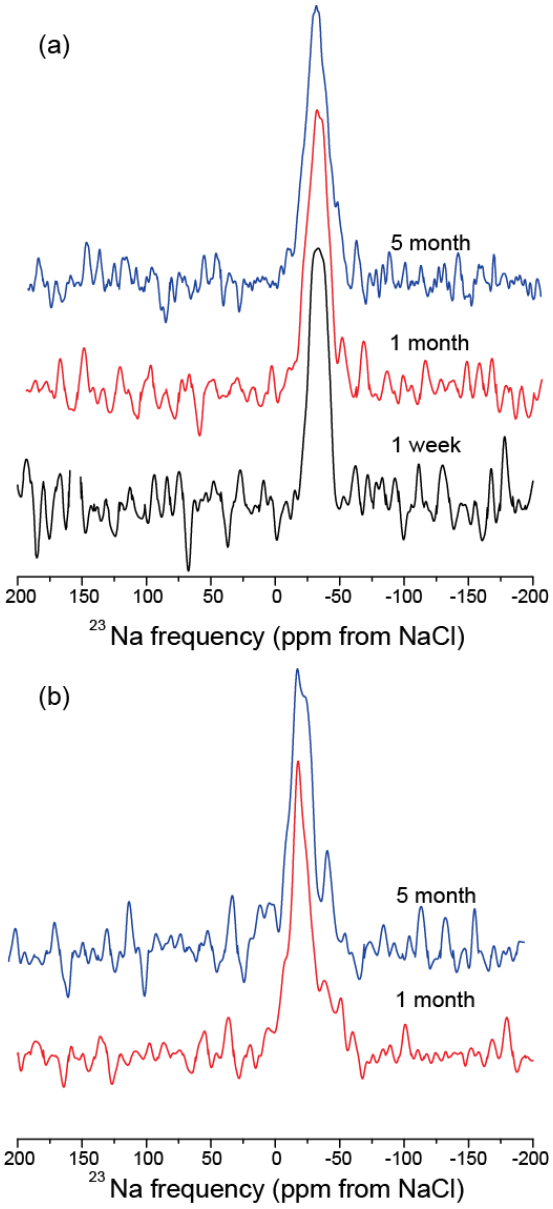

Figure 26. ^{1}H-^{23}Na CP-MAS NMR spectra of (a) SA1R and (b) AFCI. Samples were analyzed at 14.1 T with spinning speeds of 15 kHz. Spectra have been normalized to remove variation from the number of scans and sample mass.

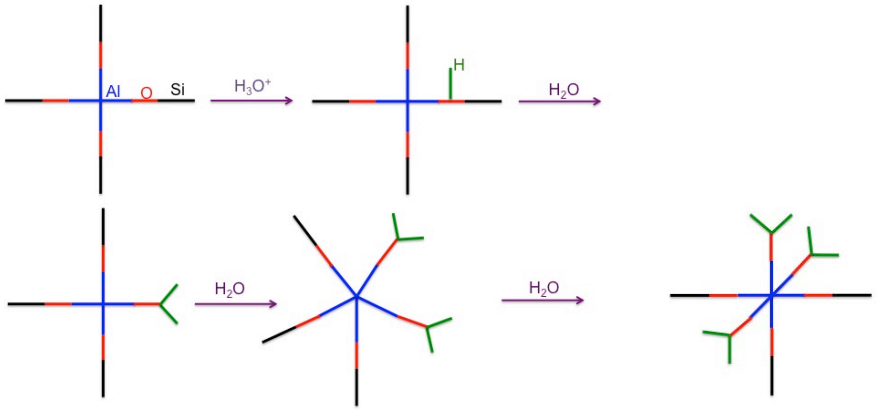

Figure 27. During hydrolysis, $^{[IV]}$Al increases coordination to form $^{[VI]}$Al, which is subsequently incorporated into the gel layer. This figure is derived from work by Criscenti et al. on the dissolution of aluminosilicates.

Changes in bonding and the structural environment may also be responsible for the nucleation of crystalline phases on highly corroded glasses. Precipitation from saturated solutions has also been considered to explain the formation of crystalline phases. In this study, crystalline phases were observed to form during the corrosion of AFCI. The presence of sharp peaks in NMR spectra indicate crystalline phases, which were observed by ^{1}H-^{29}Si CP-MAS NMR and ^{23}Na MAS NMR (Figures 5 and 9). Since the spectra of other components did not have features suggesting crystallinity, the secondary phases were identified as sodium-containing silicates. This assignment is also supported by the "quadrupolar tail" spectral feature observed for an AFCI sample (Figure 5). Otherwise, there were no features in the NMR data to suggest the nucleation of crystals within the altered layer over the time scale of these experiments.

2.4.4. Counter Diffusion Effects by Isotope Exchange and NDP

In these experiments, the possible interaction and back-diffusion of a very soluble network species, boron, was evaluated for SA1R and ISG glasses using the swapping procedure utilized for the silicon experiments. Comparable to the silicon data, the detection of ^{11}B MAS NMR signal from a glass enriched in $^{10}B_2O_3$ would indicate interaction of aqueous boron with the altered surface layer on the glass powder. Interaction of boron with the corroded ISG glass was assigned based on normalized area increases relative to the pristine $^{10}B_2O_3$ enriched glass, which had residual ^{11}B MAS NMR signal due to limitations of isotopic purities (Figures 28 and 29, Table XI). The lack of area increase for SA1R glass prevents assignment of interaction (Figures 30 and 31 and Table XII). Kim and Kirkpatrick observed the sorption of aqueous boron onto silica gel through the formation of both strong and weak surface connections, with a preferential attachment of ^{IV}B.[63] For the gels formed on ISG, ^{IV}B also preferentially attached due to the increase in normalized area for short equilibration times. As the equilibration time increased, however, ^{III}B sorption was also observed. Moreover, the chemical shifts of the ^{11}B resonances suggest B-O-B or B-O-Al connections. The sorption of boron from solution to the glass powder is an important observation since this has never been considered in general corrosion models. These reactions likely participate in the formation of the alteration layers and have implications on the glass behavior at extended corrosion times, such as the precipitation of secondary phases.

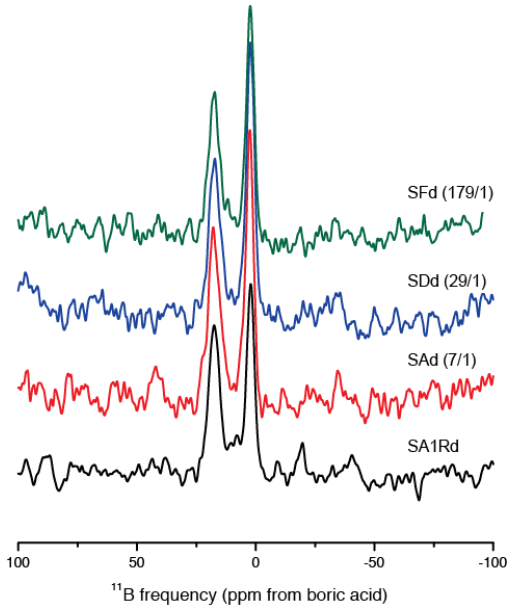

Figure 28. ^{11}B MAS NMR spectra of SA1Rd glasses containing $^{10}B_2O_3$ with a one-day equilibration time. All signal derived from these glasses results from the interaction of ^{11}B in solution with the $^{10}B_2O_3$-enriched powder or residual $^{11}B_2O_3$ in the glass. Spectra have been normalized to remove the influence of variation in the sample mass and number of scans. Samples were analyzed at 19.96 T with spinning speeds of 10 kHz.

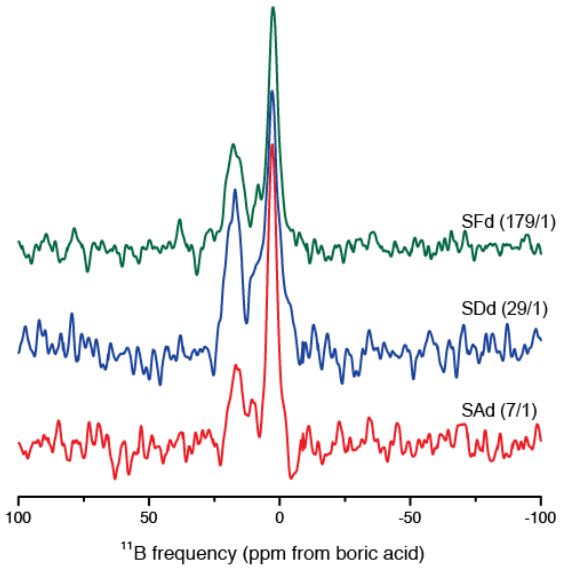

Figure 29. ^{1}H-^{11}B CP-MAS NMR spectra of SA1Rd glasses containing $^{10}B_2O_3$ with a one-day equilibration time. All signal derived from these glasses results from the dipolar interaction of ^{1}H nuclei with ^{11}B from solution that has reacted with the $^{10}B_2O_3$-enriched powder or residual $^{11}B_2O_3$ in the glass. Spectra have been normalized to remove the influence of variation in the sample mass and number of scans. Samples were analyzed at 19.96 T with spinning speeds of 10 kHz.

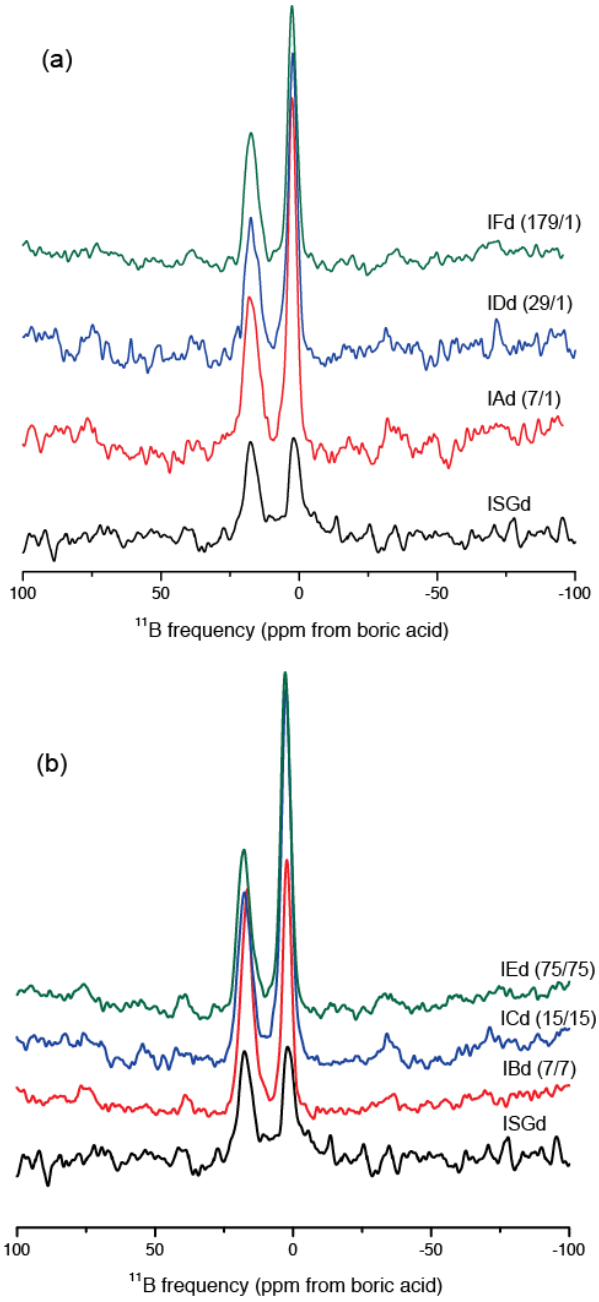

Figure 30. ^{11}B MAS NMR spectra of ISGd glasses containing in $^{10}B_2O_3$ with (a) 1-day equilibration time and (b) equivalent initial corrosion and equilibration times. All signal derived from these glasses results from the interaction of ^{11}B in solution with the $^{10}B_2O_3$-enriched powder or residual $^{11}B_2O_3$ in the glass. Spectra have been normalized to remove the influence of variation in the sample mass and number of scans. Samples were analyzed at 19.96 T with spinning speeds of 10 kHz.

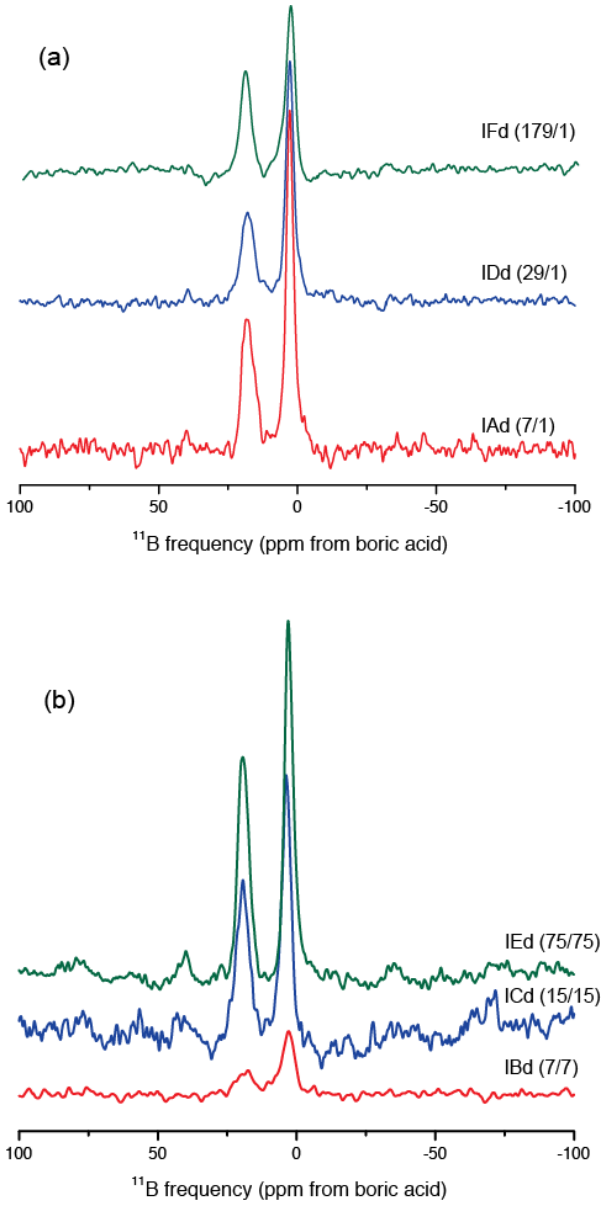

Figure 31. ^{1}H-^{11}B CP-MAS NMR spectra of ISGd glasses containing $^{10}B_2O_3$ with (a) 1-day equilibration time and (b) equivalent initial corrosion and equilibration times. All signal derived from these glasses results from the dipolar interaction of ^{1}H nuclei with ^{11}B from solution that has reacted with the $^{10}B_2O_3$-enriched powder or residual $^{11}B_2O_3$ in the glass. Spectra have been normalized to remove the influence of variation in the sample mass and number of scans. Samples were analyzed at 19.96 T with spinning speeds of 10 kHz.

Table XI. $^{III}B/^{IV}B$ ratios for $SA1R_d$ glasses, depleted in ^{11}B (containing ^{10}B). All samples had 1-day equilibration times. The total normalized area from ^{11}B MAS NMR spectra was determined by peak fitting with NUTS NMR processing software (Acorn, Inc.) for ^{10}B-containing $SA1R_d$ glasses with an equilibration time of one day. Increases in signal area relative to the pristine glass result from the interaction of ^{11}B in solution with the powder. Normalization removed differences in spectral area associated with variation in the total number of scans and sample mass.

Sample Designation	Total Normalized Area ^{III}B (X 10^4)	Total Normalized Area ^{IV}B (X 10^4)	$^{III}B/^{IV}B$ ratio
Pristine "d" glass	1.2	1.1	1.09
SA_d (7/1)	1.8	1.7	1.06
SD_d (29/1)	1.2	1.5	0.80
SF_d (179/1)	1.2	1.3	0.92

Table XII. $^{III}B/^{IV}B$ ratios for ISG_d glasses, depleted in ^{11}B (containing ^{10}B). The values in italicized font had 1-day equilibration times and the values in standard font had equivalent initial and equilibration times. The total normalized area from ^{11}B MAS NMR spectra was determined by peak fitting with NUTS NMR processing software (Acorn, Inc.) for ^{10}B-containing ISG_d glasses. Increases in signal area relative to the pristine glass result from the interaction of ^{11}B in solution with the powder. Normalization removed differences in spectral area associated with variation in the total number of scans and sample mass.

Sample Designation	Total Normalized ^{III}B Area (X 10^4)	Total Normalized ^{IV}B Area (X10^4)	$^{III}B/^{IV}B$ ratio
Pristine "d" glass	2.0	2.6	0.77
IA_d (7/1)	*3.0*	*5.3*	*0.57*
ID_d (29/1)	*2.7*	*4.8*	*0.56*
IF_d (179/1)	*2.8*	*4.1*	*0.68*
IB_d (7/7)	3.9	3.4	1.15
IC_d (15/15)	3.6	6.2	0.58
IE_d (75/75)	3.2	5.4	0.59

2.5. Thermodynamic Modeling of Saturated Glass Solutions

2.5.1. LDS Experiments

A series of dissolution experiments with simple glass compositions was undertaken to better understand the chemical characteristics of highly concentrated, alkaline solutions of dissolved silicate glasses (hereafter referred to as saturated glass solution - SGS), and especially the conditions under which the formation of crystals might occur in the presence of saturated glass solutions. It has been proposed that the resumption of high rate glass dissolution could be driven by the precipitation of certain crystalline mineral phases. Such a renewal of high rate alteration occurs at what is now defined as the transition from Stage II dissolution to Stage III dissolution, as illustrated in Figure 32 below. One of the key questions to be answered is: what solution species (ionic, molecular or oligomeric) controls this transition; ie, although a sudden drop in the concentration of several species occurs at the transition, which ones are responsible for the quasi-equilibrium during Stage II and which ones are critical to the crystallization mechanism. An understanding of these events would suggest approaches to mediate the transition. Through the use of simple glasses, thermodynamic modeling can be employed to provide a quantitative understanding that can be extended to more complex systems.

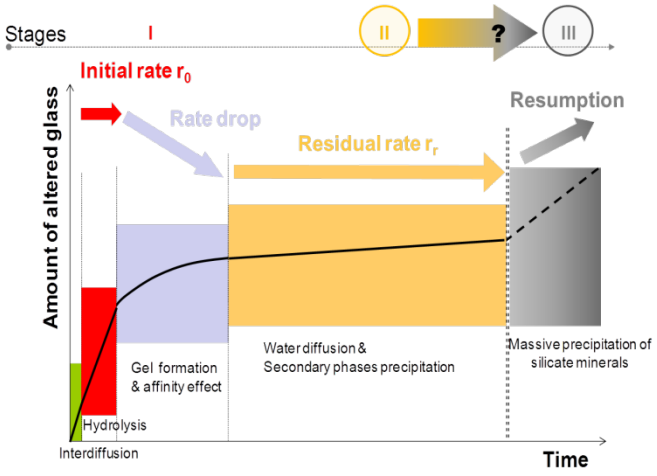

Figure 32. The transition from Stage II --> III dissolution could be caused by the thermodynamically driven precipitation of minerals from a saturated glass solution that lowers the solution concentration of certain elements such that further dissolution of the altered layer and bulk material may occur.

The titration experiments were initiated to determine the approximate maximum M/V ratio of LDS/ASTM Type I water that would lead to a total dissolution of the original starting material and not produce a precipitate material. The first two titration experiments were performed with powder that had a highly variable particle size distribution. The second set of titration experiments utilized a very-finely crushed powder in order to minimize the effects of any protective-gel layer that might form on larger particles thereby preventing a substantial amount of glass from dissolving. These experiments were also agitated in their initial stages (first 24 hours) to facilitate a greater amount of glass reacting with the solution. The ICP-AES results of the titration experiments are shown in Figure 33.

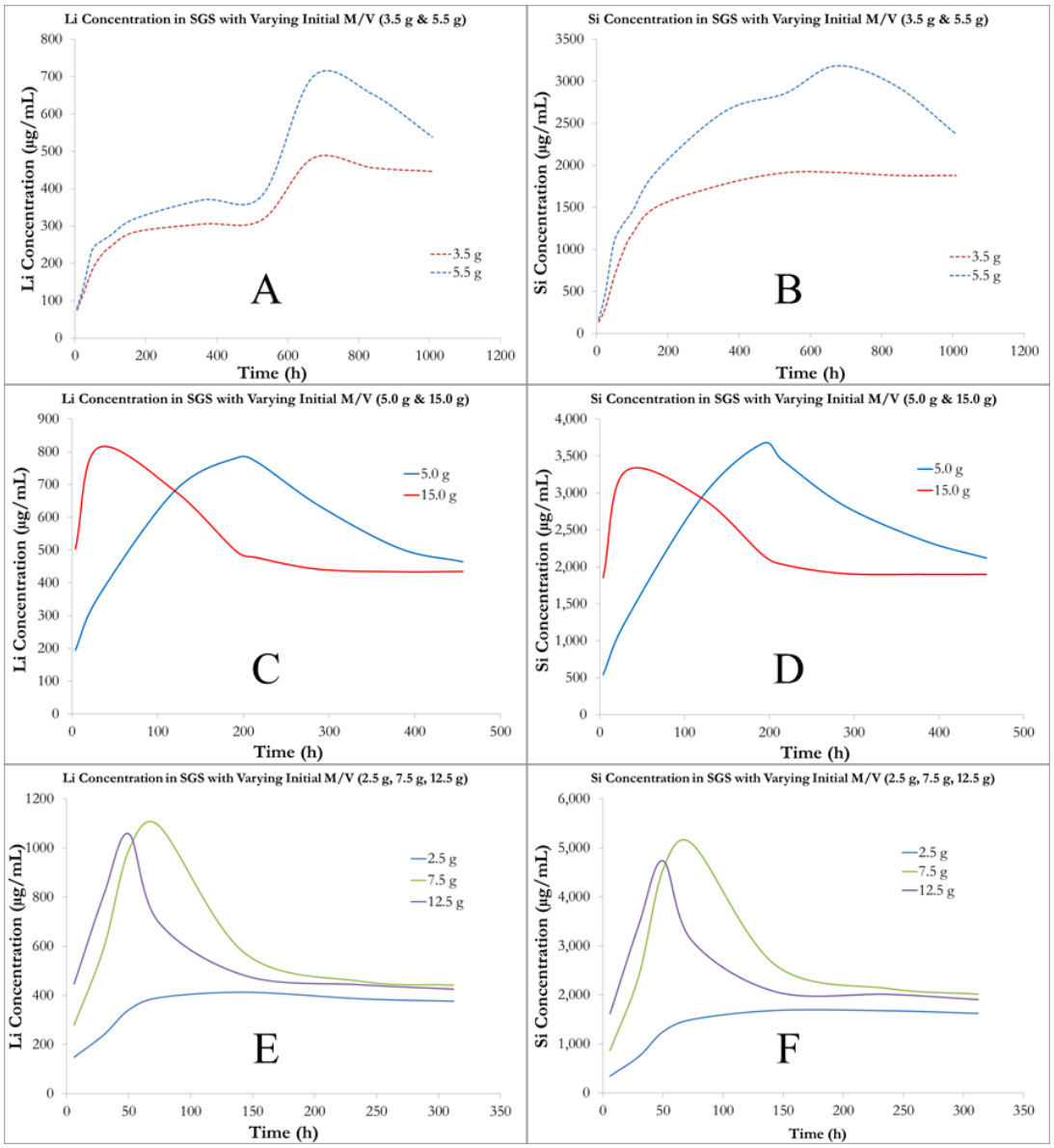

Figure 33. ICP-AES anlyses of the various titration experiments: A) Measured Li concentration for 3.5 g and 5.5 g. B) Measured Si concentration for 3.5 g and 5.5 g. C) Measured Li concentration for 5.0 g and 15.0 g. D) Measured Si concentration for 5.0 g and 15.0 g. E) Measured Li concentration for 2.5 g, 7.5 g, and 12.5 g. F) Measured Si concentration for 2.5 g, 7.5 g, and 12.5 g.

The forward dissolution rate for the first two starting masses (3.5 g and 5.5 g) was much slower than the other titration experiments and the dissolution appeared to reach a constant rate after approximately 150 h; however, after about 500 h, the dissolution rate of Li rapidly increased for both starting masses. Interestingly, the renewal of Li dissolution at ~500 h (A) did not appear to have a corresponding increase in Si concentration especially in the 3.5 g sample (B). It was also visually observed, however, that in some of the containers the larger particles were not completely dissolved. For this reason, a second and third set of titration experiments with differing masses were undertaken with very finely crushed LDS powder.

In this case, the containers were agitated to ensure that all the particles of glass in the digestion vessels reacted with the initial ASTM Type I water. This varying agitation could explain the difference in the initial rate of dissolution and maximum amount of Si and Li measured in the various SGS containers. However, all of the solutions, regardless of whether they supersaturated or not, approach a single steady state concentration for each element over time as shown in Figure 34. The only starting mass in the second and third set of titration experiments that did not super-saturate was the 2.5 g sample. No precipitate material was observed for this sample, while the final concentration of both Li and Si did not reach the apparent “equilibrium” concentrations for all the other solutions.

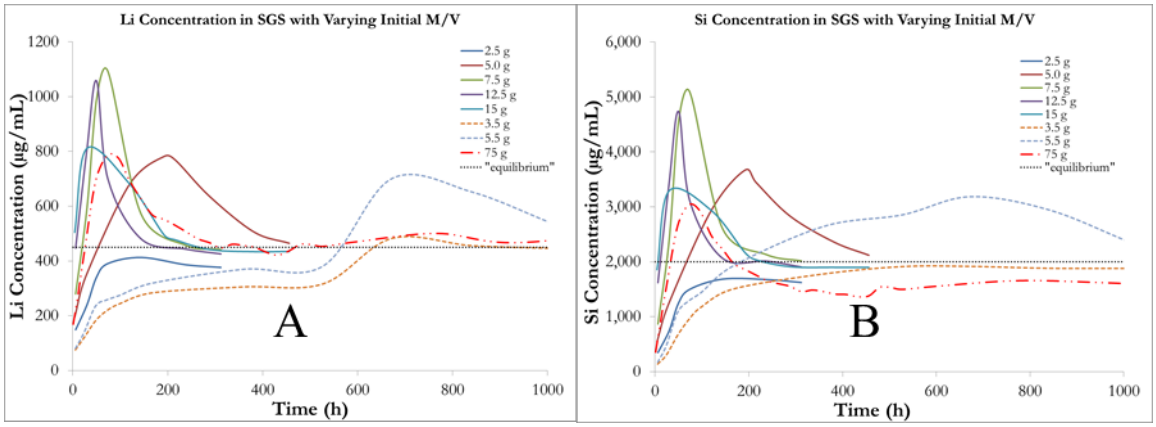

Figure 34. Solutions that reach a supersaturated concentration for both Si and Li tend to equilibrate to a single-value, steady-state concentration over time.

The results from a previous LDS experiment using an M/V ratio of 75 g / 500 mL ASTM Type I water are also included in Figure 34. While the Li concentration of this SGS approaches the hypothetical steady-state concentration, the Si concentration for this system is slightly lower than the other solutions that reached a super-saturated condition. This is likely due to differences in the starting compositions of the powder, as the glass used in the 75 g experiment was from a much earlier LDS batch than the rest of the titration experiment batches.

All of the SGS containers (except the 2.5 g) showed the eventual presence of a precipitated secondary phase. This precipitate material was examined via XRD and FESEM - the results of these measurements are shown in Figures 35 and 36, respectively.

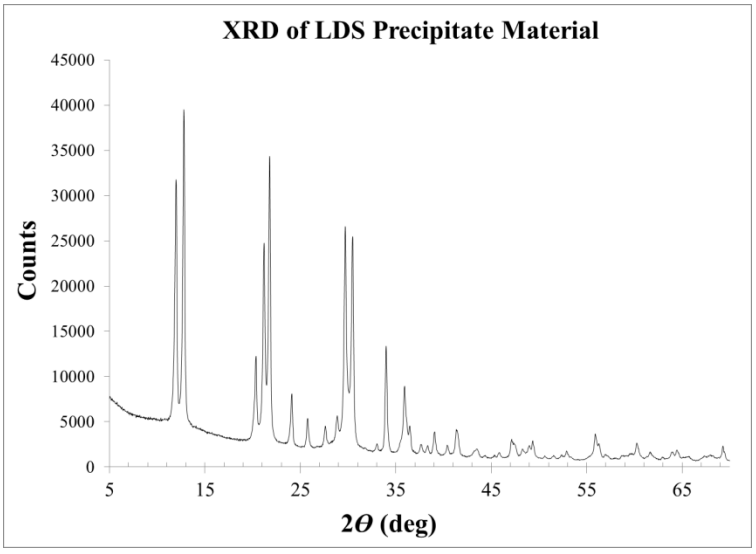

Figure 35. XRD pattern for LDS precipitate material from 75 g/500 mL SGS experiment. A hydrated lithium silicate phase is present ($Li_2Si_2O_5 \cdot 2H_2O$) along with other (as yet) unidentified peaks.

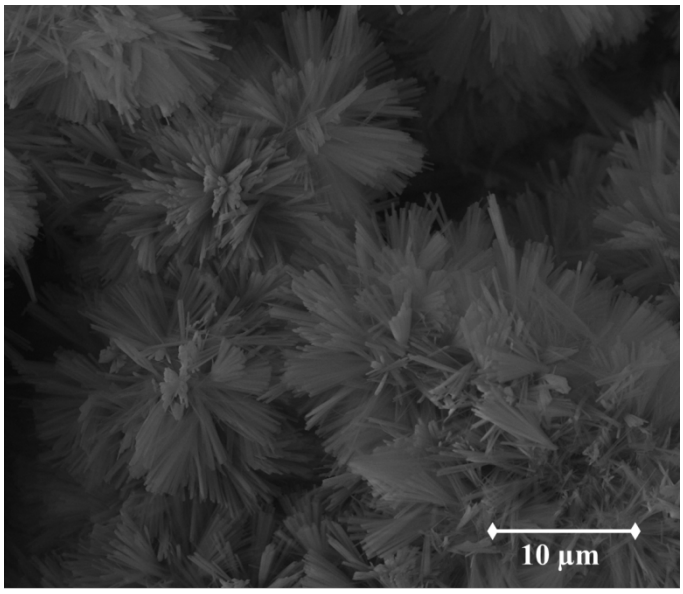

Figure 36. FESEM image of highly crystalline LDS precipitate material that was removed from the 75 g/500 mL SGS experiments after two weeks.

Another LDS SGS experiment was an attempt to determine whether precipitation of the crystals was nucleated in the gelatinous mass of gel at the bottom of the container, or was controlled entirely by the concentrated solution. This experiment employed two concentric containers, a 60 mL digestion vessel with a ported lid containing 20 g of LDS powder placed inside a 500 mL PFA jar. To date, there has been no precipitate formed in the secondary container of this vessel. But the data in Figure 37 shows a much lower Si concentration than expected for a 20g sample, suggesting that the two vessels did not equilibrate. A future experiment will employ a closed loop system and a pump to force mixing between the containers is being planned. But this initial observation strongly suggests an important role for the gel in nucleating the crystals.

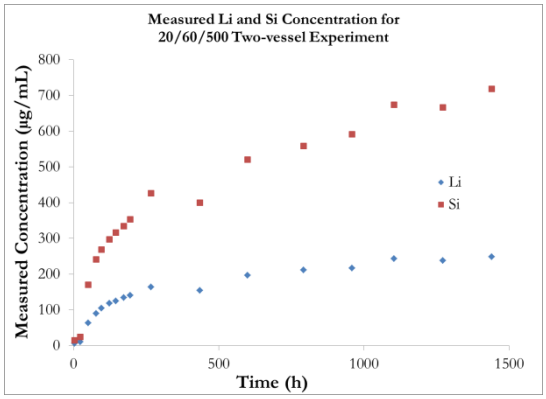

Figure 37. Measured concentrations of Li and Si in the 20/60/500 experiment using two digestion vessels, one placed inside the other. No precipitate material was observed in the secondary vessel.

2.5.2 NDS Experiments

Two experiments using various starting M/V ratios with NDS powder and ASTM Type I water were also performed. The two ratios in these experiments were chosen in an attempt to saturate the NDS SGS with respect to Na and Si concentration. Previous attempts at saturating such a solution were indeterminate. The starting ratios for the NDS experiments were 75 g/500 mL and 125 g/250 mL. The ICP-AES results of the two NDS experiments are shown in Figure 38 for their respective Na and Si concentrations.

The measured concentration for both Na and Si is much greater in the 125 g/250 mL system compared to the 75 g/500 mL system. The former system also exhibits a similar behavior to the LDS systems in that there is a rapid rise in the concentration of both the alkali and Si followed by the formation of some precipitate material in the bottom of the digestion vessel and a subsequent decrease in the concentration of both elements in solution. A similar material formed in the 75 g/ 500 mL system, but this reaction occurred over a longer period of time than in the higher M/V system. The material that formed in the NDS system appeared to be very different than the LDS material. The NDS material was much more gel-like and was not white. Some of the material from the 75 g/ 500 mL system was collected and examined with XRD, and the results of this analysis are shown in Figure 38. There are two potential matches for the NDS diffraction pattern shown in Figure 38, and both are sodium-aluminum silicates.

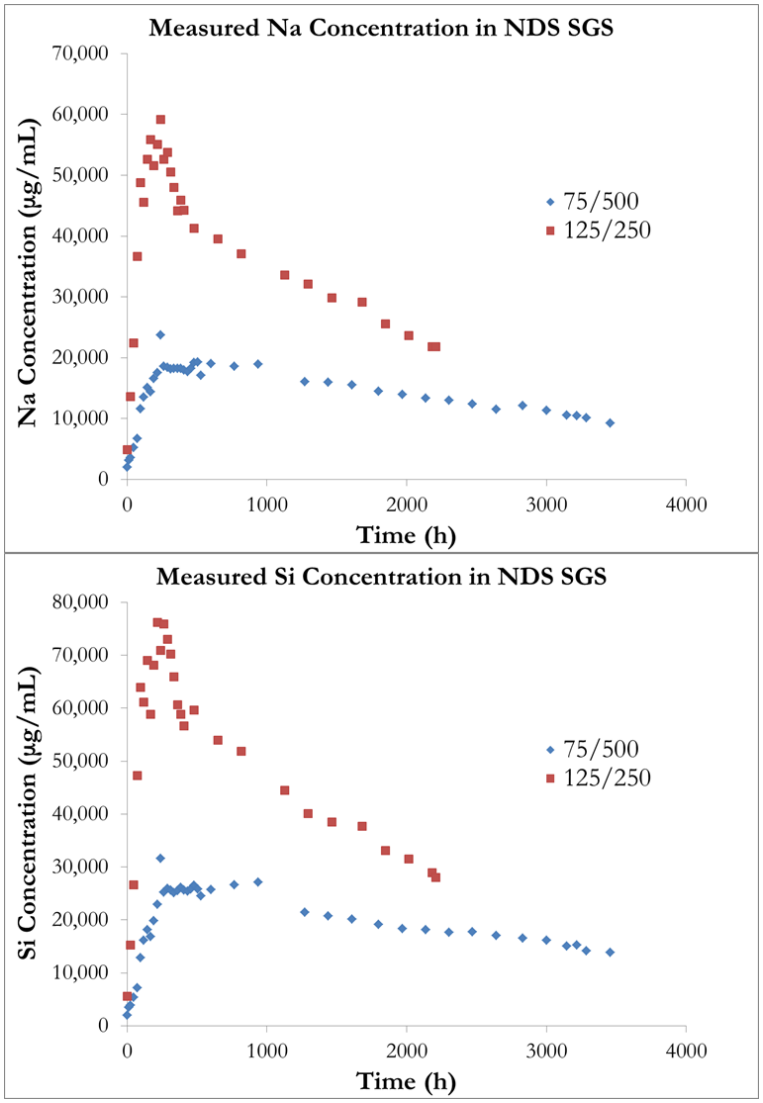

Figure 38. ICP-AES results for the two NDS SGS experiments. The 125 g/250 mL system exhibits a potential super-saturated state similar to that observed in the LDS systems before the concentration begins to drop to a steady-state value.

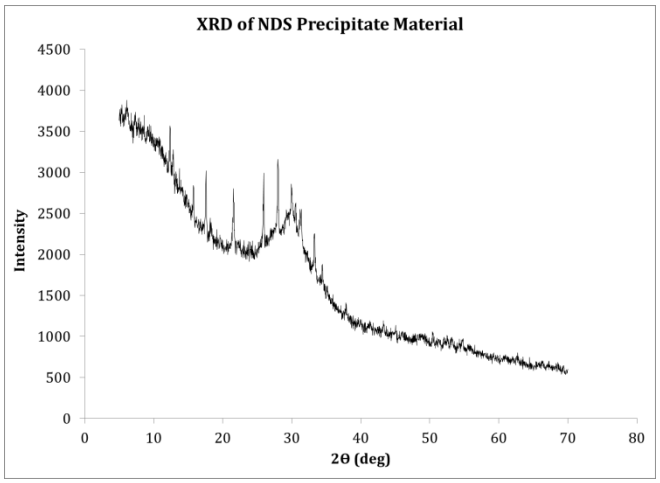

Figure 39. X-ray diffraction of precipitate material collected from the NDS system with 75 g of powder in 500 mL ASTM Type I water. The diffraction pattern shows the presence of hydrated Na-Al silicates as well as an amorphous phase.

2.5.3 Aluminum Doping Experiments

Since Al contamination was observed in several of the crystalline precipitate materials from both the NDS and LDS systems, a set of experiments was conducted to determine the effect of intentionally adding Al to an NDS and LDS system in the form of $Al(OH)_3$ after the system had reached a high enough pH value to render the hydroxide soluble (approximately 1 h). The amount of $Al(OH)_3$ that was added was such that it would yield 100 ppm Al in the SGS. The ICP-AES results of these experiments are shown in Figure 40 and Figure 41 for the LDS and NDS systems, respectively.

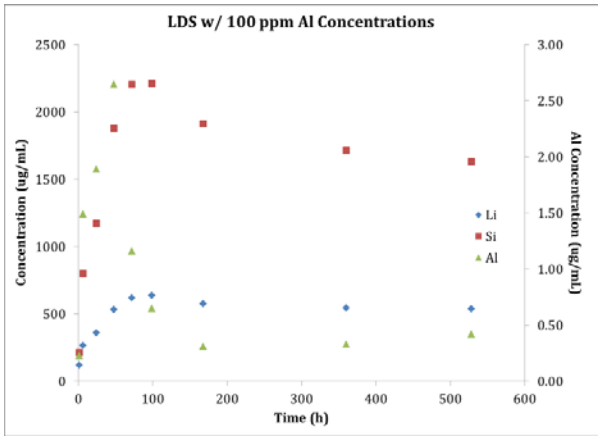

Figure 40. ICP-AES results of 150 g of LDS powder in 1000 mL of ASTM Type I water with the addition of 100 ppm Al. The concentration of Al in the SGS is shown on the secondary axis.

The dissolution of all elements in the NDS system was approximately linear and stoichiometric over the time period sampled. The LDS system, however, exhibited a similar maximum concentration of both Si and Li before starting to decrease to a residual concentration, although the maximum concentration in the Al containing system was not as high in the systems that did not have Al purposely added. We conclude that there is no effect of the Al contamination or 100ppm Al additions on the evolution of the LDS and its eventual crystallization, but there appears to be an effect on the NDS that warrants further investigation.

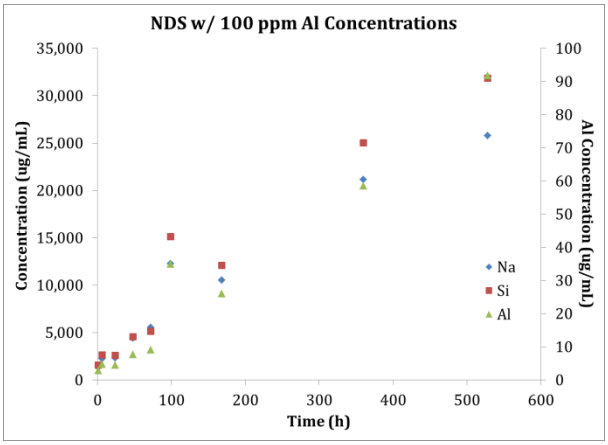

Figure 41. ICP-AES results of 150 g of NDS powder in 1000 mL of ASTM Type I water with the addition of 100 ppm Al. The concentration of Al in the SGS is shown on the secondary axis.

2.5.4 NLDS Experiments

The NLDS experiment was designed to determine if Li-based crystalline precipitates would form out of a solution that contained high sodium content given that the NDS system showed less crystallization than the LDS system. This experiment was also conducted to determine if any Na-based crystalline precipitates would form as a result of Li-crystal nucleation.

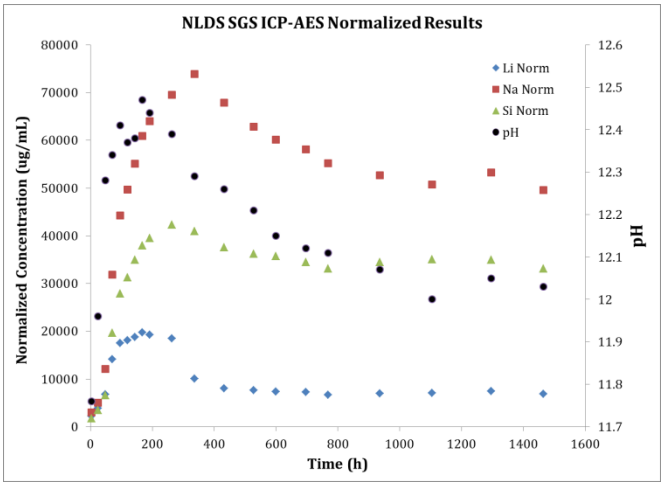

Figure 42. ICP-AES results for the NLDS system. The masses of the individual elements in solution were normalized according to the glass composition**.**

The solution analysis for the entire NLDS experiment is shown in Figure 42. The results of the ICP analysis were similar to that of the LDS experiments. The concentration of Li, Na, and Si in solution increases for a given period of time, and then decreases to a steady state (perhaps equilibrium) level in a similar fashion to the LDS system. Interestingly, the decrease in concentration is preceded by a corresponding drop in the pH value of the SGS. A highly crystalline precipitate was then observed at the bottom of the digestion jar for this NLDS system. However, it is still unclear at this time whether or not the crystallization was nucleated out of the bulk solution or from the silica gel material at the bottom of the digestion vessel. FESEM images of the crystalline formation are shown in Figure 43. EDS qualitatively showed the presence of Si, Na, O, and trace amounts of Al in these crystals (Li is not detected by EDS). Again, it is suspected that the Al contamination came from the Al_2O_3 setting plate in the oven used to anneal the NLDS glass before it was crushed into powder.

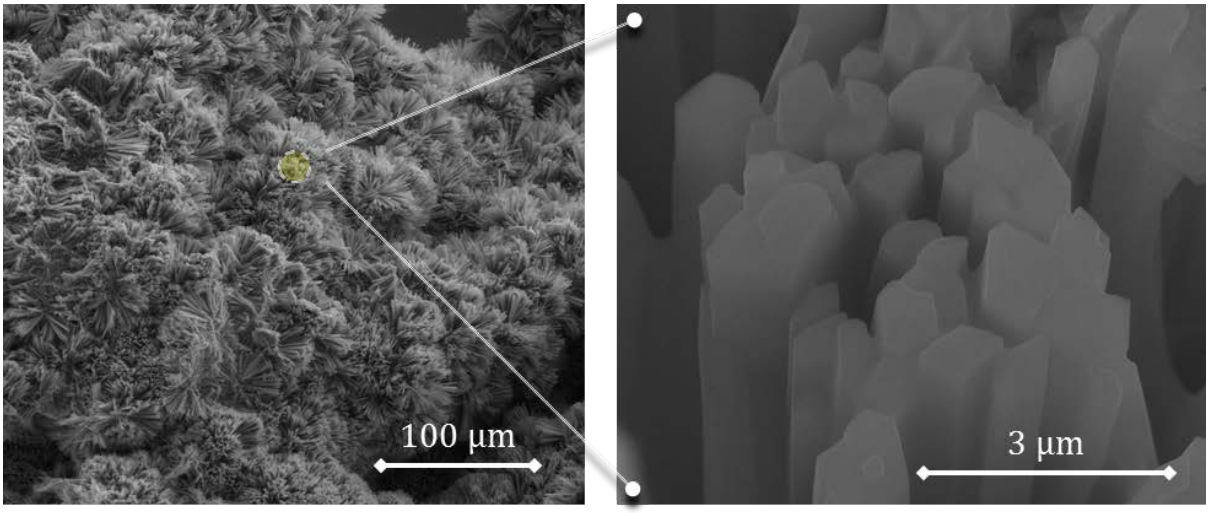

Figure 43. FESEM images showing the crystalline formations found as precipitate material at the bottom of the NLDS digestion jar. The experiment had been underway for approximately three weeks when these samples were analyzed.

In all of these SGS experiments, the mass of silica gel at the bottom of the containers (ie, relics of the leached glass particles) seemed to play a significant role in the crystallization event. To further investigate nucleation of the precipitate material, an NLDS monolith was placed on a PFA stand in the digestion vessel at the start of the experiment. The monolith was removed periodically and replaced with a fresh specimen of approximately the same size. The surfaces of the removed monoliths were examined with FESEM for precipitated material – assuming that if the precipitated material visible in the bottom of the digestion vessels was originating from the solution, the some of the precipitating material would be observable on the surface of the 'fresh' monoliths facing the top of the digestion vessel. However, no crystalline material was observed on any of the removed monoliths. The final monolith that was added to the system (at 336 hrs in Figure 42) was allowed to remain in the solution for an extended period of time. Visual observations of this monolith indicated that rather than collecting any precipitate material on its

surfaces, it was in fact shrinking in size. After a period of approximately seven to eight weeks, this 2g monolith had completely dissolved.

The total dissolution of the witness monolith (2g) should have increased the concentrations of Na, Li, and Si in the solution by at least several hundred μg/mL over the remaining course of the experiment; however, by inspection of Figure 42, it can be seen that the concentration of the elements of interest either remained constant (Li) or continued to decrease over the 1.5 month period that the monolith was observed to dissolve. This could be indicative of a steady-state condition in the solution where crystalline material is forming at the same rate glass is dissolving. But there is some uncertainty because the 2 gram sample would only increase the Si content of the SGS by 3-4% (1-2mg/ml). The experiment should be repeated with a larger monolith to validate the conclusion stated above.

2.5.5. Thermodynamic Modeling with Geochemists Workbench

Reaction path modeling was performed using the Geochemist Workbench® (GWB; Rockware, Version 9.0). The software package was composed of several sub-programs each having a specific capability. GSS was a spreadsheet input for experimental data, which was capable of computing various solution parameters ranging from cation/anion charge imbalance error to activity coefficients. REACT computes reaction path simulations using an initial solution (basis) and a geochemical process that changes it. Glass compositions were created in conjunction with laboratory dissolution experiments, LDS (33.3% Li_2O, 66.7% SiO_2) and NDS (33.3% Na_2O, 66.7% SiO_2). The thermodynamic database used was from the Lawrence Livermore National Laboratory (thermo.com.v8.r6+) and modified to include the LDS and NDS glass compositions. The glasses were arbitrarily assigned extremely high solubility constants (K_{sp}) to assure complete dissolution in the model simulations.

REACT was used to predict changes in solution chemistry based on the formation of various mineral phases. Reaction path modeling was performed by 'titrating' sequential amounts of glass into the initial basis solution, which Is similar to benign, de-ionized water (Figure 44). It was unclear which silica phase was controlling the solution chemistry, so three scenarios were examined by sequentially suppressing various silica polymorphs (SiO_2(s)) as quartz, tridymite, and SiO_2(am). Li_2SiO_3(s) and petalite were stable in all three scenarios. All three Si phases were predicted to form immediately upon glass dissolution and the predicted masses of each were relatively similar. Modeling results predicted approximately 8 g LDS dissolves into 500 mL de-ionized water, the formation of a Li_2SiO_3(s) solid phase forms (Figure 45a). As the solution becomes saturated with respect to Li_2SiO_3(s), the solution [Si] and [Li] concentrations stabilized at constant concentrations (Figure 45b and 45c).

The solubility controlled concentrations of [Si] and [Li] were dependent upon which phases were allowed to precipitate. The solubility magnitude was inversely proportional to the relative stability, or crystallinity, of the SiO_2(s) phase. For example, the most stable SiO_2 polymorphs were quartz, tridymite, and SiO_2(am), and the corresponding modeled [Si] solubility values were 1800, 2000, 4000 ppm, respectively (Figure 45b). Therefore, the early stage peaks observed in the dissolution data coincide with [Si] solubility values consistent with SiO_2(am), suggesting relatively less stable SiO_2(am) phase assemblages were important in early stage glass dissolution mechanisms. Regardless of M/V ratios, variable agitation rates or relative particle sizes, all dissolution experiments asymptotically approached a common [Si] concentration near 1800 –

2000 ppm, suggesting that late stage dissolution may be controlled by the formation of more crystalline Si phases, such as tridymite or quartz.

The addition of 100 ppm Al^{3+} had relatively little impact on the modeling prediction for Si and Li; however, petalite, a lithium-alumino-silicate ($LiAlSi_4O_{10}$), formed when 5-100 ppm Al^{3+} was added to the model. Uncertainties remain regarding kinetic limitations of petalite formation;[62] however, similar minerals were endorsed in analogous modeling efforts.[63]

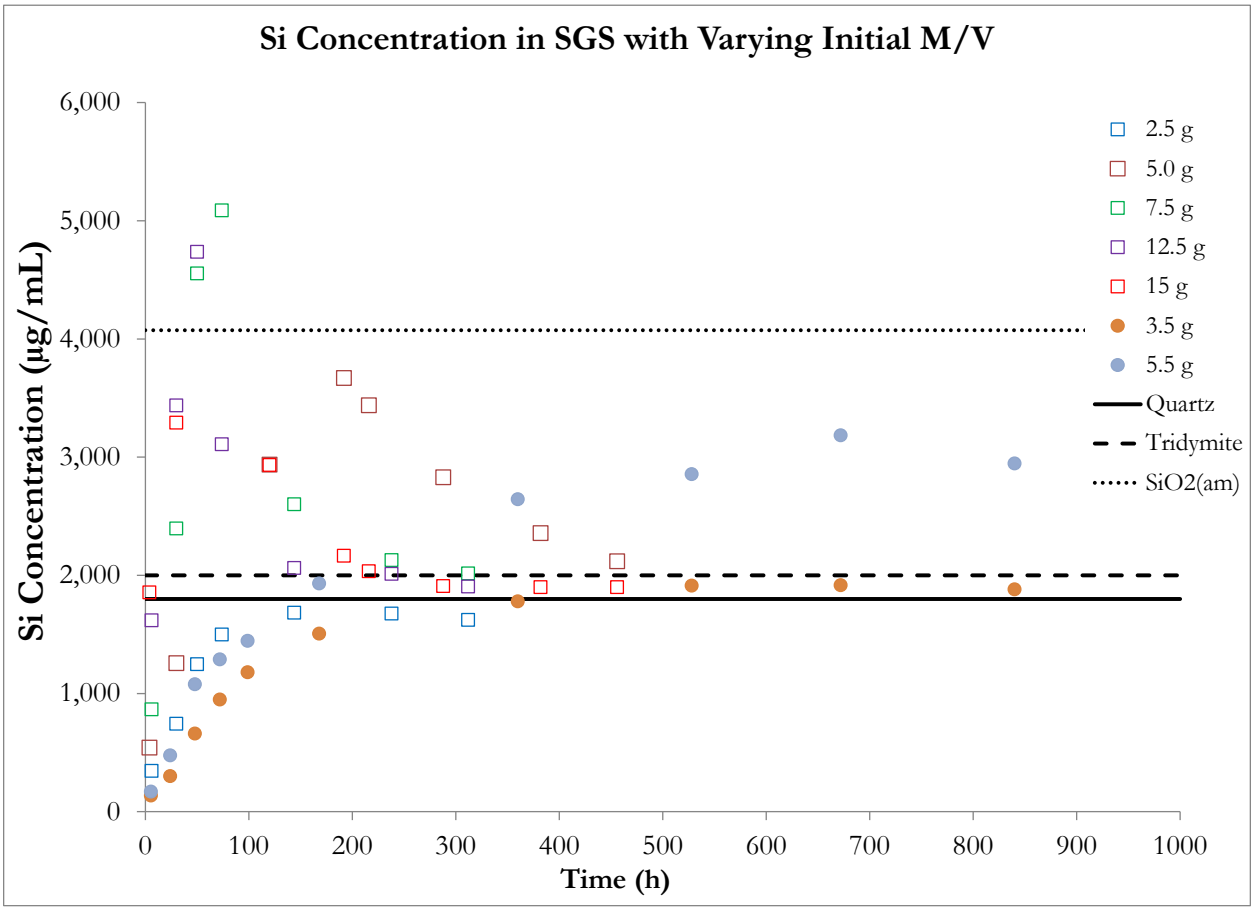

Figure 44. Si concentrations for various M/V ratios during batch glass dissolution. M/V experiments of 3.5 and 5.5 are shown as solid circles, due to the relatively large particle sizes. Open squares represent the remained of the experiments. Lines represent the [Si] solubility controlled by various SiO_2(s) polymorphs. Lines show the most stable phase (quartz, solid line), an intermediate phase (tridymite, dashed line), and least stable (SiO_2(am), dotted line).

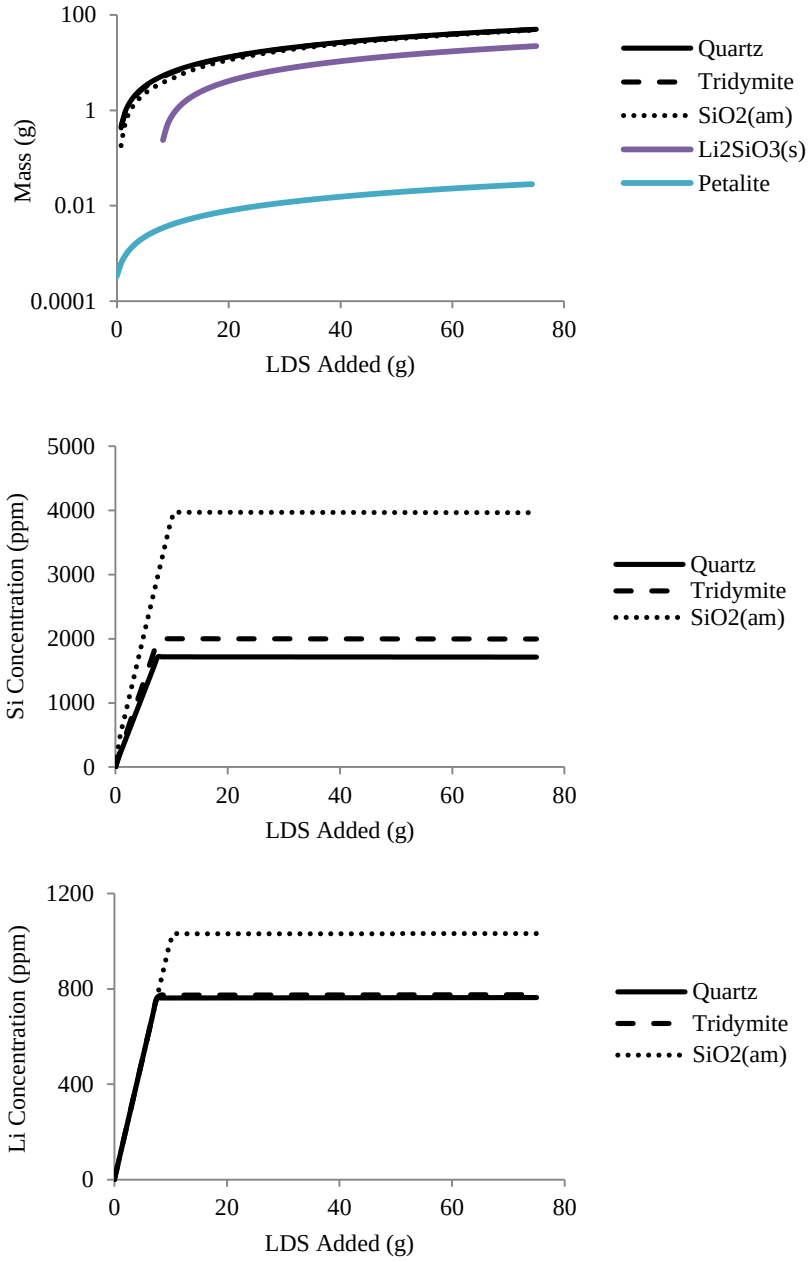

Figure 45. LDS dissolution titration GWB model and measured experimental data shown for predicted **a**. minerals (top), **b**. [Si] (middle), and **c**. [Li] (bottom). All figures are shown as a function of LDS glass sequentially added (g). Three types of SiO_2(s) phases are displayed for relative presentation purposes, yet only one was used during the model and the other two were suppressed. Li_2SiO_3(s) and petalite were stable in all three scenarios.

Reaction titration modeling for NDS predicted Si and Na concentrations at 24,840 and 20,780 ppm, respectively, for M/V ratios of 75 g/ 500 mL (Figure 46). Si and Na concentrations continually increase up to 80 g NDS added. The model predicted the formation of SiO_2(am) and analcime ($NaAlSi_2O_6*H_2O$), immediately upon addition of NDS to the initial basis solution. Measured glass dissolution data are compared to predicted Si and Na solubility's at a M/V ratio of 75 g/500 mL assuming SiO_2(am) and analcime form in solution (Figure 47). The data approach the predicted solubility's for Si and Na, suggesting SiO_2(am) and analcime control the later stage (>250 hrs) dissolution solution chemistry for NDS.

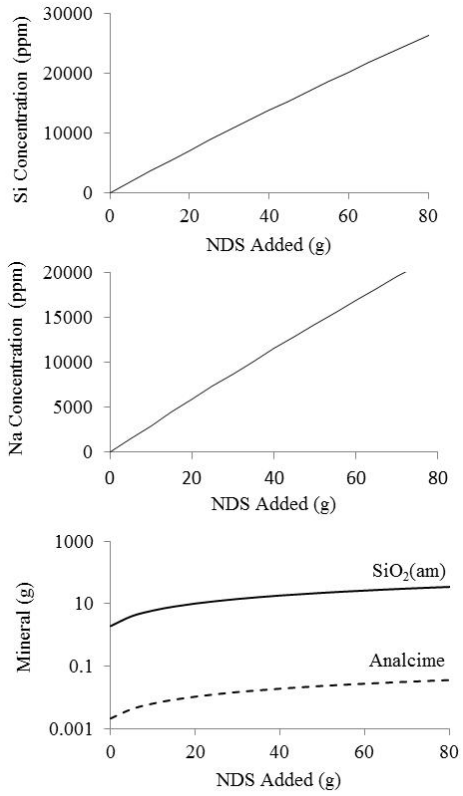

Figure 46. GWB modeling of NDS titration. Predicted Si concentrations (top), Na Concentrations (middle), and mineral phases (bottom) are shown with increasing amounts of NDS.

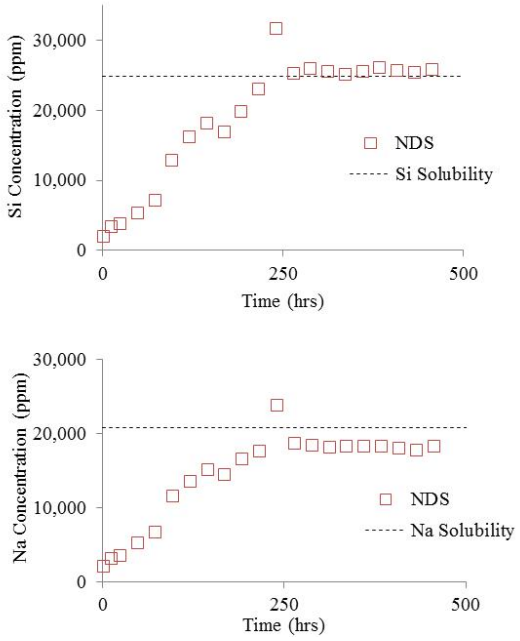

Figure 47. Dissolution data from NDS (squares) and modeled solubility (dashed) of Si (upper) and Na (lower).

2.6. NMR Database

One of the objectives of this work was to generate a database of research that is accessible to scientists in the nuclear waste glass field. In order to accomplish this task and also adhere to quality assurance, we utilized LabTrove. LabTrove is an online electronic notebook/blogging tool that was created by groups at the University of Southampton. We have worked in collaboration with the developers to improve this tool. The freedom provided by LabTrove allows the user to adopt multiple organization techniques, ensuring that data is approachable even for individuals unfamiliar with the experiments conducted. LabTrove offers collaborators and other interested parties the ability to make comments and suggestions in "real-time" as the experiments are conducted. Currently, our LabTrove is private so only users we approve can access the information. As the project comes to a close, we will make the database open to a wider audience. An image of the interface is presented in Figure 31.

Figure 48. Image of user interface for LabTrove blogging tool.

3.0 Conclusions

NMR is not an intrinsically surface analytical technique, and so it was necessary to work with very high surface area powdered samples. This limited our ability to know the spatial distribution of the detected signal. The inability to analyze samples containing Fe (with the equipment available) limited the NMR studies to Fe-free glasses. Nevertheless, the NMR data provided information about local coordination structure and the dynamics of exchange between glass and solution that is not available with most other methods. The future use of fibers can alleviate the problem of spatial distribution because the thickness and composition of the altered surface layers can be independently measured before the fibers are subjected to NMR analysis.

The study of saturated glass solutions was motivated by several aspects of this study. First, the use of an exceedingly high surface-area-to-volume ratio raised important questions about the leachate and its interaction with the glass. Second, the isotope exchange experiments showed that the gel, itself, warranted further studies, but for NMR it would require almost fully leached glass. The SGS approach successfully yielded gelatinous glass particles that were suitable for NMR analysis; these samples are still of interest and will be evaluated in the future. Third, and perhaps now of most interest, the SGS approach may be a convenient way to test the hypothesis that crystallization of one or more phases at long times could be responsible for the resumption of high rate dissolution. The results presented are promising, but were confined to simple binary and ternary glasses of poor durability. It needs to be shown that similar characteristics appear in the case of the more durable wasteform glasses. Once validated, the SGS approach could provide a way to more rapidly screen glasses for improved performance.

4.0 Publications

Cory L Trivelpiece, John J. Petrunis, Carlo G. Pantano, and R. Gregory Downing, "Glass Surface Layer Density by Neutron Depth Profiling", Int. J. of Glass Science, 3[2] pp. 137-143 (2012).

K.A. Murphy, N.M. Washton, J.V. Ryan, C.G. Pantano, K.T. Mueller, "*Solid-State NMR Examination of Alteration Layers on a Nuclear Waste Glass.*" *J. Non-Cryst. Solids*. 2013. 369: 44-54.

K.A. Murphy, N.M. Washton, J.V. Ryan, C.G. Pantano, K.T. Mueller, "*Monitoring the Formation of Surface Layers by Si-29 Isotopic Tracing* and Solid-State NMR." to be submitted to *ACS Appl. Mater. Interfaces*

K.A. Murphy, N.M. Washton, J.V. Ryan, C.G. Pantano, K.T. Mueller, "*The Re-entrance of Aqueous Boron Into Nuclear Waste Glass Powders*." to be submitted to *IJAGS*

A. Leone, C. Trivelpiece, K.A. Murphy, K.T. Mueller and C.G. Pantano, "*Leaching and Altered Layer Formation on Fibers versus Powder"***,** to be submitted.

C. Trivelpiece and C.G. Pantano, "*NDP Analysis of Alkali-Ion Counter Diffusion during the Leaching of Glass at High pH*", in preparation

C. Trivelpiece, L. Larson, K.A. Murphy, K.T. Mueller and C.G. Pantano, "Thermodynamic Modeling of Saturated Glass Solutions and Gels", in preparation

5.0 References

(1) Van Iseghem, P.; Aertsens, M.; Gin, S.; Deneele, D.; Grambow, B.; McGrail, P.; Strachan, D.; Wicks, G. 2007.
(2) Bergeron, B.; Galoisy, L.; Jollivet, P.; Angeli, F.; Charpentier, T.; Calas, G.; Gin, S. *Journal of Non-Crystalline Solids* **2010**, *356*, 2315.
(3) Cailleteau, C.; Angeli, F.; Devreux, F.; Gin, S.; Jestin, J.; Jollivet, P.; Spalla, O. *Nature Materials* **2008**, *7*, 978.
(4) Gin, S.; Guittonneau, C.; Godon, N.; Neff, D.; Rebiscoul, D.; Cabie, M.; Mostefaoui, S. *Journal of Physical Chemistry C* **2011**, *115*, 18696.
(5) Rebiscoul, D.; Rieutord, F.; Ne, F.; Frugier, P.; Cubitt, R.; Gin, S. *Journal of Non-Crystalline Solids* **2007**, *353*, 2221.
(6) Pierce, E. M.; Rodriguez, E. A.; Calligan, L. J.; Shaw, W. J.; McGrail, B. P. *Applied Geochemistry* **2008**, *23*, 2559.
(7) Strachan, D. M.; Croak, T. L. *Journal of Non-Crystalline Solids* **2000**, *272*, 22.
(8) Neeway, J.; Abdelouas, A.; Grambow, B.; Schumacher, S. *Journal of Nuclear Materials* **2011**, *415*, 31.
(9) Ferrand, K.; Abdelouas, A.; Grambow, B. *Journal of Nuclear Materials* **2006**, *355*, 54.
(10) Grambow, B.; Muller, R. *Journal of Nuclear Materials* **2001**, *298*, 112.
(11) Gin, S.; Jegou, C.; Frugier, P.; Minet, Y. *Chemical Geology* **2008**, *255*, 14.

(12) Aagaard, P.; Helgeson, H. C. *American Journal of Science* **1982**, *282*, 237.
(13) Oelkers, E. H. *Geochimica Et Cosmochimica Acta* **2001**, *65*, 3703.
(14) Lodding, A. R.; Engstrom, E. U.; Zoitos, B. K.; Clark, D. E.; Wicks, G. G. *Journal of the American Ceramic Society* **1992**, *75*, 2702.
(15) Lodding, A.; Van Iseghem, P. *Journal of Nuclear Materials* **2001**, *298*, 197.
(16) Curti, E.; Crovisier, J. L.; Morvan, G.; Karpoff, A. M. *Applied Geochemistry* **2006**, *21*, 1152.
(17) Gong, W. L.; Wang, L. M.; Ewing, R. C.; Vernaz, E.; Bates, J. K.; Ebert, W. L. *Journal of Nuclear Materials* **1998**, *254*, 249.
(18) Pelegrin, E.; Calas, G.; Ildefonse, P.; Jollivet, P.; Galoisy, L. *Journal of Non-Crystalline Solids* **2010**, *356*, 2497.
(19) Ribet, S.; Gin, S. *Journal of Nuclear Materials* **2004**, *324*, 152.
(20) Valle, N.; Verney-Carron, A.; Sterpenich, J.; Libourel, G.; Deloule, E.; Jollivet, P. *Geochimica Et Cosmochimica Acta* **2010**, *74*, 3412.
(21) Hamilton, J. P.; Pantano, C. G. *Journal of Non-Crystalline Solids* **1997**, *222*, 167.
(22) Tsomaia, N.; Brantley, S. L.; Hamilton, J. P.; Pantano, C. G.; Mueller, K. T. *American Mineralogist* **2003**, *88*, 54.
(23) Conradt, R. *Journal of the American Ceramic Society* **2008**, *91*, 728.
(24) Angeli, F.; Gaillard, M.; Jollivet, P.; Charpentier, T. *Geochimica Et Cosmochimica Acta* **2006**, *70*, 2577.
(25) Frugier, P.; Gin, S.; Minet, Y.; Chave, T.; Bonin, B.; Godon, N.; Lartigue, J. E.; Jollivet, P.; Ayral, A.; De Windt, L.; Santarini, G. *Journal of Nuclear Materials* **2008**, *380*, 8.
(26) Curti, E.; Dahn, R.; Farges, F.; Vespa, M. *Geochimica Et Cosmochimica Acta* **2009**, *73*, 2283.
(27) Jollivet, P.; Angeli, F.; Cailleteau, C.; Devreux, F.; Frugier, P.; Gin, S. *Journal of Non-Crystalline Solids* **2008**, *354*, 4952.
(28) Cailleteau, C.; Devreux, F.; Spalla, O.; Angeli, F.; Gin, S. *Journal of Physical Chemistry C* **2011**, *115*, 5846.
(29) Chave, T.; Frugier, P.; Ayral, A.; Gin, S. *Journal of Nuclear Materials* **2007**, *362*, 466.
(30) Gin, S.; Jegou, C.; Vernaz, E. *Applied Geochemistry* **2000**, *15*, 1505.
(31) Gin, S.; Ribet, I.; Couillard, M. *Journal of Nuclear Materials* **2001**, *298*, 1.
(32) Gin, S.; Mestre, J. P. *Journal of Nuclear Materials* **2001**, *295*, 83.
(33) Gin, S.; Beaudoux, X.; Angeli, F.; Jegou, C.; Godon, N. *Journal of Non-Crystalline Solids* **2012**, *358*, 2559.
(34) Jollivet, P.; Frugier, P.; Parisot, G.; Mestre, J. P.; Brackx, E.; Gin, S.; Schumacher, S. *Journal of Nuclear Materials* **2012**, *420*, 508.
(35) Frugier, P.; Chave, T.; Gin, S.; Lartigue, J. E. *Journal of Nuclear Materials* **2009**, *392*, 552.
(36) Ebert, W. L.; Fortner, J. A.; Billings, A. L.; Crawford, C. **2011**.
(37) Poinssot, C.; Gin, S. *Journal of Nuclear Materials* **2012**, *420*, 182.
(38) Martin, C.; Ribet, I.; Frugier, P.; Gin, S. *Journal of Nuclear Materials* **2007**, *366*, 277.
(39) Neeway, J.; Abdelouas, A.; Grambow, B.; Schumacher, S.; Martin, C.; Kogawa, M.; Utsunomiya, S.; Gin, S.; Frugier, P. *Journal of Non-Crystalline Solids* **2012**, *358*, 2894.
(40) Rebiscoul, D.; van der Lee, A.; Frugier, P.; Ayral, A.; Gin, S. *Journal of Non-Crystalline Solids* **2003**, *325*, 113.
(41) Rebiscoul, D.; Van der Lee, A.; Rieutord, F.; Ne, F.; Spalla, O.; El-Mansouri, A.; Frugier, P.; Ayral, A.; Gin, S. *Journal of Nuclear Materials* **2004**, *326*, 9.

(42) Vernaz, E.; Gin, S.; Jegou, C.; Ribet, I. *Journal of Nuclear Materials* **2001**, *298*, 27.
(43) Guittonneau, C.; Gin, S.; Godon, N.; Mestre, J. P.; Dugne, O.; Allegri, P. *Journal of Nuclear Materials* **2011**, *408*, 73.
(44) Donzel, N.; Gin, S.; Augereau, F.; Ramonda, M. *Journal of Nuclear Materials* **2003**, *317*, 83.
(45) Crum, J. V.; Billings, A. L.; Lang, J.; Marra, J. C.; Rodriguez, C.; Ryan, J. V.; Vienna, J. D. *Baseline Glass Development for Combined Fission Products Waste Streams, **AFCI-WAST-WAST-MI-DV-2009-000075***, Pacific Northwest National Laboratory, 2009.
(46) ASTM International: West Conshohocken, PA, 2002.
(47) Fyfe, C. A.; Feng, Y.; Grondey, H.; Kokotailo, G. T.; Gies, H. *Chemical Reviews* **1991**, *91*, 1525.
(48) Nanba, T.; Asano, Y.; Benino, Y.; Sakida, S.; Miura, Y. *Physics and Chemistry of Glasses-European Journal of Glass Science and Technology Part B* **2009**, *50*, 301.
(49) Doremus, R. H. *Journal of Non-Crystalline Solids* **1975**, *19*, 137.
(50) Doremus, R. H.; Mehrotra, Y.; Lanford, W. A.; Burman, C. *Journal of Materials Science* **1983**, *18*, 612.
(51) Crovisier, J. L.; Advocat, T.; Dussossoy, J. L. *Journal of Nuclear Materials* **2003**, *321*, 91.
(52) Zhou, Z.; Fyfe, W. S. *American Mineralogist* **1989**, *74*, 1045.
(53) Jercinovic, M. J.; Keil, K.; Smith, M. R.; Schmitt, R. A. *Geochimica Et Cosmochimica Acta* **1990**, *54*, 2679.
(54) Hellmann, R.; Eggleston, C. M.; Hochella, M. F.; Crerar, D. A. *Geochimica Et Cosmochimica Acta* **1990**, *54*, 1267.
(55) Bunker, B. C.; Tallant, D. R.; Headley, T. J.; Turner, G. L.; Kirkpatrick, R. J. *Physics and Chemistry of Glasses* **1988**, *29*, 106.
(56) Peck, J. A.; Farnan, I.; Stebbins, J. F. *Geochimica Et Cosmochimica Acta* **1988**, *52*, 3017.
(57) Casey, W. H.; Westrich, H. R.; Arnold, G. W. *Geochimica Et Cosmochimica Acta* **1988**, *52*, 2795.
(58) Casey, W. H.; Westrich, H. R.; Arnold, G. W.; Banfield, J. F. *Geochimica Et Cosmochimica Acta* **1989**, *53*, 821.
(59) Criscenti, L. J.; Brantley, S. L.; Mueller, K. T.; Tsomaia, N.; Kubicki, J. D. *Geochimica Et Cosmochimica Acta* **2005**, *69*, 2205.
(60) Ostwald, W. *Zeitschrift fur Physikalische Chemie* **1897**, *22*, 289.
(61) Jantzen, C. M.; Brown, K. G.; Pickett, J. B. *International Journal of Applied Glass Science* **2010**, *1*, 38.
(62) Černý, P.; London, D. *Tschermaks mineralogische und petrographische Mitteilungen*, **1983,** 31(1-2), 81.
(63) Skorski, D. C., Ryan, J. V., Strachan, D. M., & Lepry, W. C. (**2011**). *Engineering Glass Passivation Layers-Model Results (No. PNNL-20615),* Pacific Northwest National Laboratory (PNNL), Richland, WA (US).